An *in silico*-based investigation on anisotropic hyperelastic constitutive models for soft biological tissues

Hüsnü Dal[1,2], Alp Kağan Açan[1,2], Ciara Durcan[3] and Mokarram Hossain[3]

[1]Department of Mechanical Engineering, Middle East Technical University, Çankaya, Ankara , Türkiye.
[2]Computational Micromechanics Laboratory, CAD/CAM Robotics Center, Middle East Technical University, Çankaya, Ankara , Türkiye.
[3]Zienkiewicz Institute for AI, Data and Modelling, Swansea University, Swansea, SA1 8EN, United Kingdom.

Abstract

We review twelve invariant and dispersion-type anisotropic hyperelastic constitutive models for soft biological tissues based on their fitting performance to various experimental data. To this end, we used a hybrid multi-objective optimization procedure along with a genetic algorithm to generate the initial guesses followed by a gradient-based search algorithm. The constitutive models are then fit to a set of uniaxial and biaxial tension experiments conducted on tissues with different histology. For the *in silico* investigation, experiments conducted on human aneurysmatic abdominal aorta, linea alba, and rectus sheath tissues are utilized. Accordingly, the models are ranked with respect to an objective normalized quality of fit metric. Finally, a detailed discussion is carried out on the fitting performance of the models. This work provides a valuable quantitative comparison of various anisotropic hyperelastic models, the findings of which can aid researchers in selecting the most suitable constitutive model for their particular analysis. The investigation reveals superior fitting performance of dispersion-type anisotropic constitutive formulations over invariant formulations.

Keywords: soft biological tissues, collagen distribution, anisotropy, constitutive modelling

1 Introduction

To successfully model the physiological functions of soft tissues and to investigate any pathophysiology, the constitutive models that are used to analytically capture the mechanical behavior of biological tissues are essential and form the basis for computational models to study organ/tissue function on structural level. Baseline hyperelasticity is a precursor to the modeling of more advanced phenomena such as viscoelasticity [14], electroelasticity [21] and electro-viscoelasticity [12, 13, 73, 74] in mechanics of soft biological tissues.

It has previously been well established that soft tissues respond elastically to a given force and past a certain point, i.e. under large strains, behave nonlinearly [8, 30, 94]. Hyperelasticity, similar to that observed for rubbery polymers, is

---

[*] Corresponding author: Hüsnü Dal Email: dal@metu.edu.tr

required [55, 87]. Unlike rubbery polymers, which commonly have an isotropic material composition, biological tissues are generally observed to be anisotropic. This is mainly due to dispersion, i.e. nonuniformity of the angular distribution of the collagen fibers [64]. Animal tissues may provide a qualitative description for human tissues, but the data from such experiments cannot be used to accurately model human tissues, especially for biomedical applications. Despite being less prevalent than animal studies, there are also a wide variety of experimental studies on human soft tissues, with investigations being conducted both *in vivo* and *ex vivo*. In this work, we will focus purely on human data from *ex vivo* experiments as these allow for large deformations that clearly display the nonlinear elastic behavior of the tissues. Experimental data for healthy human soft tissues can be found for the brain [11], spleen [63], skin [39], aorta [29, 93], bile duct [37], oesophagus [25–27], GI tract [28], liver [91], cervical tissue [78], while also for diseased tissues such as aneurysmatic aortas [86] and diabetic foot plantar tissues [81]. Nonuniformity of geometric distribution of fibers account for nonlinear stress-strain behaviour in soft biological tissues.

The anisotropic hyperelastic response of soft biological tissues can be described in terms of Helmholtz free-energy function or the so-called strain-energy density function (SEDF). Various forms of SEDFs can be classified into three main groups; based on (i) Green-Lagrange strain components [31, 57, 88, 89], (ii) anisotropic invariants [56], and (iii) fiber dispersion [64, 65]. The first generic free-energy function in terms of Green-Lagrange strain components was proposed by Tong and Fung [89]. Then, 2D and 3D extensions were made by Fung et al. [18, 31], see also [17, 62, 88, 92] for subsequent developments. The main drawbacks of these models are; (i) they have large number of material parameters, and (ii) such models are purely phenomenological (material parameters possess no physical meaning) and exclude micro-structural information related to the histology of tissues. Furthermore, such models may easily violate the convexity condition [44] unless material parameters are not selected carefully. On contrary, the invariant-based approach considers the direction of the mean fiber family and takes into account the stretch of fibers via an anisotropic invariant. A number of the models based on invariants were proposed with different forms of the free-energy function, e.g. in polynomial form [52, 59, 77], in power form [7, 36], and in exponential form [44, 50, 71, 94]. The invariant-based models assume that fibers are perfectly aligned, however, collagen fibers exist in a dispersed form inside the tissue. The first model taking into account the dispersion of fibers was first presented by Lanir [64]. Therein, he proposed a continuum framework to model flat biological tissues using an *angular integration* approach by considering the dispersion of collagen and elastin fibers. Following the work of Lanir, several angular integration (AI) based anisotropic constitutive models have been proposed over the years [1, 2, 4, 24, 83, 96]. For example, the approach of Sacks [83] incorporates planar collagen fiber distribution directly obtained from *small angle light scattering* (SALS) technique. Zulliger et al. [96] utilizes log-logistic distribution for planar dispersion of collagen in arterial wall. Alastrue et al. incorporated π-periodic von Mises [1] and Bingham [2] distribution and proposed a constitutive framework based on numerical integration over a unit micro-sphere, respectively. Another class of constitutive models arise from the so-called *generalized structural tensor* (GST) approach. The AI based models, on the one hand, take into account the mechanical response in an orientation direction and obtain the macroscopic response in an integral representation, On the other hand, the GST approaches make use of a macro-kinematic tensor, or the so-called the generalized structure tensor that results from the integration of the fiber density distribution. Within this context, Gasser et al. [34] proposed a GST approach with a single dispersion parameter motivated by planar von-Mises density distribution function. This approach was further extended by Holzapfel et al. [46] to include out-of-plane dispersion of fibers by using two scalar dispersion parameters motivated by bivariate von Mises distribution function. The GST approach can be considered as a first order Taylor series expansion of a dispersed fibers around a mean direction [82]. Pandolfi & Vasta proposed a second order model that generalizes GST approach. The model recovers the AI and GST approaches for highly aligned (low dispersion) fibers, whereas it corrects the mechanical response of the GST approach towards the AI-based formulation for more dispersed fiber distribution scenarios.

Soft biological tissues exhibit strong tension-compression asymmetry, since the thin fibres easily buckle when subjected to compression [3, 66]. It is usually assumed that an isotropic base matrix exhibit tension-compression symmetry and anisotropic contribution, mostly emanating from collagen content contributes merely to tensile mechanical loads [45, 47, 67]. For tissues having highly aligned collagen fibers (low dispersion), imposition of tension only condition for invariant and GST-based approaches are numerically more accurate and tractable [75]. However, for more dispersed fiber distributions, excluding the contribution of fibers under compression requires more sophisticated numerical treatment [69, 75].

A number of comprehensive reviews have been carried out on the topic of hyperelastic constitutive models [20, 53, 54, 87]. Besides seminal works of Fung [32], Humphrey [57, 58], see also references [15, 42]. For specific reviews, we refer to [76] for brain and fat tissues, [9] for intestine, [95] for abdominal organs, [61] for skin, [34] for arterial wall, [49] for dispersion-type anisotropic models, among others. The aforementioned reviews exclude a one-to-one quantitative comparison of models used for soft tissues. In this work, we outline the derivation of stress expressions for invariant- and dispersion-type models, discuss some of the constitutive models in literature, and carry out an *in silico* investigation to compare performance of various models to capture the anisotropic hyperelastic behavior of three distinct human tissues. The data for this is obtained from experimental studies of aortic aneurysms and different regions of the healthy abdominal wall. This work provides a detailed framework of how to utilize the constitutive models, while also providing an in-depth critical analysis of each models' performance ability according to different data sets and loading domains. The findings of this review can be used in research or industry to support and inform the selection of the best constitutive model for a specific soft tissue application.

We pursue our investigation based on the datasets proposed by Niestrawska et al. [79], Cooney et al. [19], and Martins et al. [70] for abdominal aortic aneurysm (AAA) tissue, the linea alba and the rectus sheath, respectively. AAA is a pathological condition of the abdominal aorta which results in local bulging, while the linea alba and rectus sheath are sections of the abdominal wall. The overall output of the paper is twofold. Firstly, the applicability of each constitutive model to a particular type of tissue will be assessed, specifically the aptness of various anisotropic

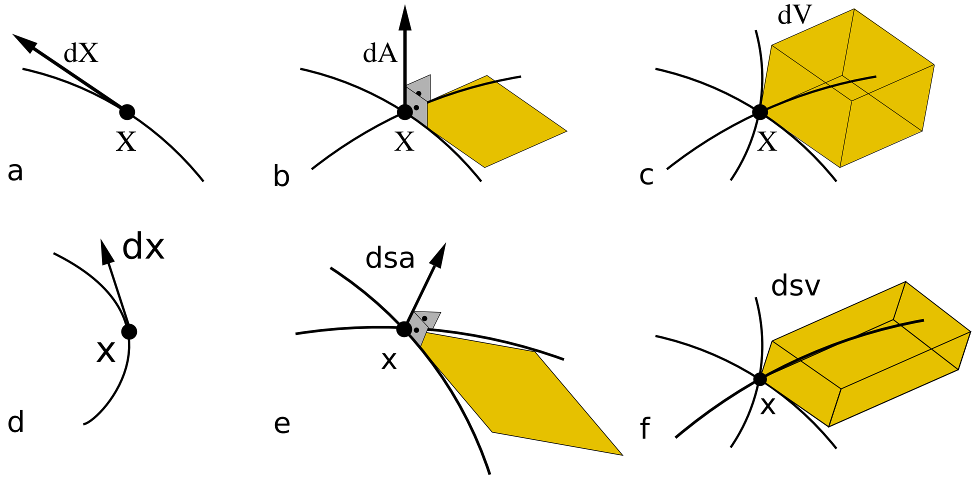

Fig. 1 Three fundamental maps of a continuum: The deformation gradient $\boldsymbol{F}$ as a mapping of an infinitesimal line element in (a) undeformed configuration and (d) deformed configuration, its cofactor cof$[\boldsymbol{F}]$ as an area map (b) in undeformed configuration and (e) deformed configuration, its determinant det$[\boldsymbol{F}]$ as a volume map in (c) undeformed configuration and (f) deformed configuration.

fiber distribution functions to the three tissues mentioned above. Secondly, the fitting performance of various dispersion-type anisotropic constitutive models will be compared. In this study, we will

- outline twelve anisotropic hyperelastic models and derive the closed form stress expressions for the uniaxial tension (UT) and equibiaxial tension (ET) deformation states based on the classical incompressibility assumption,
- implement the aforementioned constitutive models into a hybrid genetic-gradient search algorithm outlined in Dal et al. [20],
- identify the material parameters of each model (i) with respect to an ET dataset for AAA tissue [79], (ii) a UT dataset for the linea alba [19], and (iii) a UT dataset for the rectus sheath [70],
- sort all the models with respect to an objective *quality of fit* metric according to their fitting performance to the AAA tissue dataset [79], the linea alba dataset [19], and the rectus sheath dataset [70].
- identify parameters and the quality of fit values of each constitutive model in tabular form. Also, the stress-strain curves for each constitutive model will be provided in separate graphs.

The paper is organized as follows: the mathematical preliminaries for the kinematics of incompressible anisotropic hyperelastic solids are presented in Section 2. In Section 3, tweleve anisotropic hyperelastic constitutive models for soft biological tissues are summarized. Section 4 outlines the experimental procedures for the characterization of the quasi-static hyperelastic response of the soft human tissues selected in this study. Moreover, the parameter identification procedure and the quality of fit metric are provided. Finally, a detailed discussion of the results is presented in Section 5.

2 Fundamentals of hyperelastic deformable solids

In this section, the kinematics, state variables and stress expressions for an anisotropic hyperelastic continuum will be introduced. The mathematical framework of invariant and dispersion-type anisotropic hyperelastic formulations will be briefly

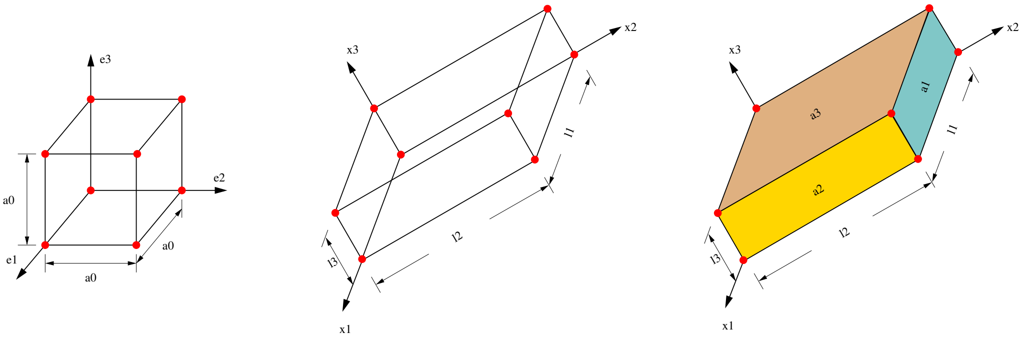

Fig. 2 The invariants (a) $I_1(\boldsymbol{C}) = \lambda_1^2 + \lambda_2^2 + \lambda_3^2$ as the sum of squares of the principal stretches, (b) $I_2(\boldsymbol{C}) = \nu_1^2 + \nu_2^2 + \nu_3^2$ as the sum of squares of principal areal stretches, where $\nu_i = J/\lambda_i$, and (c) $I_3 = J^2 = \lambda_1^2\lambda_2^2\lambda_3^2$ as the square of the volumetric stretch [22].

discussed. For a more detailed treatment of the subject, we refer to the monographs [33, 43], *inter alia.*

2.1 Geometric mappings and the field variables

2.1.1 Kinematics

Let the deformation map $\boldsymbol{\varphi}(\boldsymbol{X}, t)$ represent the motion of a deformable solid body. It maps the reference/Lagrangian configuration $\boldsymbol{X} \in \mathscr{B}_0$ of material points onto the current/Eulerian configuration of material points $\boldsymbol{x} = \boldsymbol{\varphi}_t(\boldsymbol{X})$ at time $t \in \mathscr{T} \subset \mathbb{R}_+$. The *deformation gradient* $\boldsymbol{F} = \nabla\boldsymbol{\varphi}$ maps the unit tangent of the reference configuration onto the spatial counterpart. In this sequence, let line, area, and volume elements in the Lagrangian configurations to be denoted as $d\boldsymbol{X}$, $d\boldsymbol{A}$, dV, respectively. The Eulerian counterparts of these elements are obtained through the deformation gradient $\boldsymbol{F}$, its cofactor $\mathrm{cof}[\boldsymbol{F}] = \det[\boldsymbol{F}]\boldsymbol{F}^{-T}$ and its Jacobian $J := \det[\boldsymbol{F}]$

$$d\boldsymbol{x} = \boldsymbol{F}d\boldsymbol{X}\ , \qquad d\boldsymbol{a} = \mathrm{cof}[\boldsymbol{F}]d\boldsymbol{A}\ , \qquad dv = \det[\boldsymbol{F}]dV\ , \tag{1}$$

see also Figure 1. $J := \det[\boldsymbol{F}] > 0$ guarantees the nonpenetrable deformations. Moreover, the *right Cauchy-Green tensor* is related to the deformation gradient by $\boldsymbol{C} = \boldsymbol{F}^T\boldsymbol{F}$.

2.1.2 Principal stretches and invariants

The principle of material objectivity and the principle of frame indifference require that the energy stored in the hyperelastic material be a function of either principal stretches or invariants of the right Cauchy-Green tensor. The spectral decomposition of right Cauchy-Green tensor and its cofactor reads

$$\boldsymbol{C} := \sum_{a=1}^{3} \lambda_a^2 \boldsymbol{N}^a \otimes \boldsymbol{N}^a \quad \text{and} \quad \mathrm{cof}[\boldsymbol{C}] := \sum_{a=1}^{3} \nu_a^2 \boldsymbol{N}^a \otimes \boldsymbol{N}^a\,, \tag{2}$$

where

$$\nu_i = J/\lambda_i \quad \text{with} \quad \nu_1 = \lambda_2\lambda_3\,, \quad \nu_2 = \lambda_3\lambda_1\,, \quad \nu_3 = \lambda_1\lambda_2\,, \tag{3}$$

are the *principal areal stretches*, see Figure 2. Moreover, the three isotropic invariants of the right Cauchy-Green tensor are

$$I_1 := \mathrm{tr}[\boldsymbol{C}], \quad I_2 := \mathrm{tr}[\mathrm{cof}[\boldsymbol{C}]], \quad \text{and} \quad I_3 := \det[\boldsymbol{C}]\,. \tag{4}$$

The principal stretches and the invariants of the right Cauchy-Green tensor are related as

$$I_1 = \lambda_1^2 + \lambda_2^2 + \lambda_3^2, \quad I_2 = \nu_1^2 + \nu_2^2 + \nu_3^2, \quad I_3 = J^2 = \lambda_1^2\lambda_2^2\lambda_3^2\,. \tag{5}$$

For an infinitesimal cubic element, the three isotropic invariants of the right Cauchy-Green stretch tensor are associated with *linear*, *areal*, and *volumetric* stretches in the principal directions. Let the Lagrangian unit vectors $\boldsymbol{M}_1$ and $\boldsymbol{M}_2$ denote the orientation directions of two fiber families for the description of the anisotropic behavior of soft tissues. These vectors can be represented using spherical coordinates, as shown in the Figure 3, as follows

$$\boldsymbol{M}_i = M_{i1}\boldsymbol{e}_1 + M_{i2}\boldsymbol{e}_2 + M_{i3}\boldsymbol{e}_3 \quad \text{with} \quad i = 1, 2\,. \tag{6}$$

where $M_{i1} = \sin\theta\cos\phi$, $M_{i2} = \sin\theta\sin\phi$, and $M_{i3} = \cos\theta$. If the fibers are symmetrical around the $\boldsymbol{e}_1$ direction and lies on the $\boldsymbol{e}_1$-$\boldsymbol{e}_2$ plane as observed in the arterial tissue, the preferred fiber directions can be written as follows

$$\boldsymbol{M}_i = \cos\varphi\boldsymbol{e}_1 \pm \sin\varphi\boldsymbol{e}_2 \quad \text{with} \quad i = 1, 2\,, \tag{7}$$

where φ is the angle between the fiber and the symmetry axis $\boldsymbol{e}_1$. Two additional invariants that take into account the contribution of a single family of fiber alignment $\boldsymbol{M}_1$ are defined as

$$I_4 := \boldsymbol{M}_1 \cdot \boldsymbol{C}\boldsymbol{M}_1 \qquad \text{and} \qquad I_5 := \boldsymbol{M}_1 \cdot \boldsymbol{C}^2\boldsymbol{M}_1\;. \tag{8}$$

For an additional family of fibers identified via mean orientation $\boldsymbol{M}_2$, two additional invariants are described

$$I_6 := \boldsymbol{M}_2 \cdot \boldsymbol{C}\boldsymbol{M}_2 \qquad \text{and} \qquad I_7 := \boldsymbol{M}_2 \cdot \boldsymbol{C}^2\boldsymbol{M}_2\;. \tag{9}$$

where $\lambda_1^f = \sqrt{I_4}$ and $\lambda_2^f = \sqrt{I_6}$ represent the stretches of the fibers in the orientation directions $\boldsymbol{M}_1$ and $\boldsymbol{M}_2$, respectively. For some specific tissue, the two families of fibers might interact with one another. This requires the use of additional coupling invariant

$$I_8 := (\boldsymbol{M}_1 \cdot \boldsymbol{C}\boldsymbol{M}_2)(\boldsymbol{M}_1 \cdot \boldsymbol{M}_2) \tag{10}$$

Here, the unit orientation vectors of two families of fibers, symmetrically disposed in the $\boldsymbol{e}_1 - \boldsymbol{e}_2$ plane in current configuration are

$$\boldsymbol{m}_1 = \boldsymbol{F}\boldsymbol{M}_1 \qquad \text{and} \qquad \boldsymbol{m}_2 = \boldsymbol{F}\boldsymbol{M}_2\;. \tag{11}$$

Moreover, the second order structure tensors can be defined as

$$\boldsymbol{A}_1 = \boldsymbol{M}_1 \otimes \boldsymbol{M}_1 \qquad \text{and} \qquad \boldsymbol{A}_2 = \boldsymbol{M}_2 \otimes \boldsymbol{M}_2\;. \tag{12}$$

2.2 Free-energy function and the stress expressions

Hyperelastic materials are governed by a potential function, the Helmholtz free-energy function that describes the energy stored as a result of mechanical deformation. Polymeric materials and soft biological tissues exhibit a distinct response to bulk deformation and shear-type deformations. In this context, it is common practice to split the deformation into dilatational and volume-preserving parts [60]

$$\boldsymbol{F} = \boldsymbol{F}_{\text{vol}}\bar{\boldsymbol{F}} \quad \text{with} \quad \boldsymbol{F}_{\text{vol}} := J^{1/3}\mathbf{1}\,. \tag{13}$$

The corresponding deformation measure reads

$$\boldsymbol{C} = (J^{2/3}\mathbf{1})\bar{\boldsymbol{C}} \quad \text{with} \quad \bar{\boldsymbol{C}} = \bar{\boldsymbol{F}}^T\bar{\boldsymbol{F}}\,. \tag{14}$$

Based on (13) and (14), the free-energy function is expressed as

$$\Psi(\boldsymbol{F},\boldsymbol{A}_1,\boldsymbol{A}_2) = U(J) + \bar{\Psi}(\bar{\boldsymbol{F}},\boldsymbol{A}_1,\boldsymbol{A}_2) \tag{15}$$

where $U(J)$ and $\bar{\Psi}(\bar{\boldsymbol{F}},\boldsymbol{A}_1,\boldsymbol{A}_2)$ represent the volumetric and isochoric response of the material, respectively. Further decomposition of the isochoric free-energy function was suggested by Holzapfel and Weizsacker [51]. They proposed decomposition of the free-energy function into isotropic and anisotropic parts,

$$\bar{\Psi}(\bar{\boldsymbol{F}},\boldsymbol{A}_1,\boldsymbol{A}_2) = \bar{\Psi}_{\text{iso}}(\bar{\boldsymbol{F}}) + \bar{\Psi}_{\text{ani}}(\bar{\boldsymbol{F}},\boldsymbol{A}_1,\boldsymbol{A}_2)\,. \tag{16}$$

The wavy collagen fibers do not store energy under contractile deformations [4, 45, 66]. Hence, the isotropic ground matrix is active $\bar{\Psi}_{\text{iso}}$ under small deformations. On contrary, the collagen fibers dominate the overall behavior at high stretch levels governed by $\bar{\Psi}_{\text{ani}}$ [44]. Following the arguments of Gültekin et al. [40, 41] on the use of the invariants of the total deformation, we employ the specific form of the free-energy function

$$\Psi(\boldsymbol{F},\boldsymbol{A}_1,\boldsymbol{A}_2) = U(J) + \tilde{\Psi}(\boldsymbol{F},\boldsymbol{A}_1,\boldsymbol{A}_2) \tag{17}$$

where

$$\tilde{\Psi}(\boldsymbol{F},\boldsymbol{A}_1,\boldsymbol{A}_2) = \Psi_{\text{iso}}(\boldsymbol{F}) + \Psi_{\text{ani}}(\boldsymbol{F},\boldsymbol{A}_1,\boldsymbol{A}_2)\,. \tag{18}$$

Herein, the $\bar{\boldsymbol{F}}$ is replaced with $\boldsymbol{F}$ for the sake of convenience. [1] Recall that, in the incompressible limit, the formulations (15) and (17) lead to identical results. In this investigation, the volumetric part of the free-energy function $U(J)$ will be excluded and the pressure term will be obtained from boundary conditions by enforcing exactly the incompressible deformation state under uniaxial and biaxial deformations. A canonical relation between the stresses and the free-energy function can be established in the sense

$$\boldsymbol{P} := \partial_{\boldsymbol{F}}\tilde{\Psi} = \boldsymbol{F}\boldsymbol{S}\ , \quad \boldsymbol{S} = 2\partial_{\boldsymbol{C}}\hat{\Psi}(\boldsymbol{C},\boldsymbol{A}_1,\boldsymbol{A}_2)\ , \quad \text{and} \quad \boldsymbol{\tau} = \boldsymbol{F}\boldsymbol{S}\boldsymbol{F}^T \tag{19}$$

where $\boldsymbol{P}$, $\boldsymbol{S}$ and $\boldsymbol{\tau}$ are the first Piola-Kirchhoff stress tensor, second Piola-Kirchhoff stress tensor, and the Kirchhoff stress tensor, respectively. $\hat{\psi}(\boldsymbol{C},\boldsymbol{A}_1,\boldsymbol{A}_2)$ is the alternative representation of the free-energy function (18) in terms of the right Cauchy-Green tensor. Thereafter, the Lagrangian moduli expression result from the second derivative of $\hat{\Psi}$ with respect to $\boldsymbol{C}$,

$$\mathbb{C} = 4\partial^2_{\boldsymbol{C}\boldsymbol{C}}\hat{\Psi}(\boldsymbol{C},\boldsymbol{A}_1,\boldsymbol{A}_2)\ . \tag{20}$$

---

[1] In the subsequent treatment, the biological tissues will be assumed to behave perfectly incompressible.

2.2.1 Invariant-based anisotropic hyperelastic formulations

The Lagrangian and Eulerian stresses for invariant-based formulations of anisotropic elasticity result from the application of the chain rule

$$\boldsymbol{S} = 2\partial_{\boldsymbol{C}}\Psi = 2\sum_{i=1}^{7}\frac{\partial\Psi}{\partial I_i}\frac{\partial I_i}{\partial \boldsymbol{C}}\,. \tag{21}$$

The closed form expressions for the Lagrangian and Eulerian stress tensors (21) require the following derivatives

$$\begin{aligned} \partial_{\boldsymbol{C}} I_1 &= \boldsymbol{1}\,, & \partial_{\boldsymbol{C}} I_2 &= I_1\boldsymbol{1} - \boldsymbol{C}\,, \quad \partial_{\boldsymbol{C}} J = \tfrac{1}{2}\,J\boldsymbol{C}^{-1}\,, \\ \partial_{\boldsymbol{C}} I_4 &= \boldsymbol{A}_1\,, & \partial_{\boldsymbol{C}} I_5 &= \boldsymbol{M}_1\otimes\boldsymbol{C}\boldsymbol{M}_1 + \boldsymbol{M}_1\boldsymbol{C}\otimes\boldsymbol{M}_1\,, \\ \partial_{\boldsymbol{C}} I_6 &= \boldsymbol{A}_2\,, & \partial_{\boldsymbol{C}} I_7 &= \boldsymbol{M}_2\otimes\boldsymbol{C}\boldsymbol{M}_2 + \boldsymbol{M}_2\boldsymbol{C}\otimes\boldsymbol{M}_2\,. \end{aligned} \tag{22}$$

Substitution of (22) into $(21)_1$ gives the invariant-based representation for the second Piola-Kirchhoff stress tensor[2]

$$\begin{aligned} \boldsymbol{S} &= 2\psi_1\boldsymbol{1} + 2\psi_4\boldsymbol{A}_1 + 2\psi_5(\boldsymbol{M}_1\otimes\boldsymbol{C}\boldsymbol{M}_1 + \boldsymbol{M}_1\boldsymbol{C}\otimes\boldsymbol{M}_1) \\ &\quad + 2\psi_6\boldsymbol{A}_2 + 2\psi_7(\boldsymbol{M}_2\otimes\boldsymbol{C}\boldsymbol{M}_2 + \boldsymbol{M}_2\boldsymbol{C}\otimes\boldsymbol{M}_2) - p\boldsymbol{C}^{-1}\,. \end{aligned} \tag{23}$$

The push-forward of the second Piola-Kirchhoff stress leads to the invariant-based representation for the Kirchhoff stress expression

$$\begin{aligned} \boldsymbol{\tau} &= 2\psi_1\,\boldsymbol{b} + 2\psi_4(\boldsymbol{m}_1\otimes\boldsymbol{m}_1) + 2\psi_5(\boldsymbol{m}_1\otimes\boldsymbol{b}\boldsymbol{m}_1 + \boldsymbol{m}_1\boldsymbol{b}\otimes\boldsymbol{m}_1) \\ &\quad + 2\psi_6(\boldsymbol{m}_2\otimes\boldsymbol{m}_2) + 2\psi_7(\boldsymbol{m}_2\otimes\boldsymbol{b}\boldsymbol{m}_2 + \boldsymbol{m}_2\boldsymbol{b}\otimes\boldsymbol{m}_2) - p\boldsymbol{1}\,, \end{aligned} \tag{24}$$

with $\psi_i = \dfrac{\partial\Psi}{\partial I_i}$ and $p = -J\partial_J U$. The stress expressions given in (23) and (24) can be expressed in terms of index notation for the principal directions[3] and $\boldsymbol{m}_i$ for the fiber family # i, respectively.

$$\begin{aligned} S_i &= 2\psi_1 \quad + 2\psi_4 M_{1i}^2 + 4\psi_5 M_{1i}^2\lambda_i^2 + 2\psi_6 M_{2i}^2 + 4\psi_7 M_{2i}^2\lambda_i^2 - \frac{1}{\lambda_i^2}p\,, \\ \tau_i &= 2\psi_1\lambda_i^2 + 2\psi_4 m_{1i}^2 + 4\psi_5 m_{1i}^2\lambda_i^2 + 2\psi_6 m_{2i}^2 + 4\psi_7 m_{2i}^2\lambda_i^2 - p\,. \end{aligned} \tag{25}$$

Furthermore, moduli expression (20) can be additively decomposed into isotropic and anisotropic parts as follows $\mathbb{C} = \mathbb{C}_{\text{iso}} + \mathbb{C}_{\text{ani}}$ where

$$\mathbb{C}_{\text{iso}} = 4\partial^2_{\boldsymbol{C}\boldsymbol{C}}\Psi_{\text{iso}}(\boldsymbol{C},\boldsymbol{A}_1,\boldsymbol{A}_2) \quad \text{and} \quad \mathbb{C}_{\text{ani}} = 4\partial^2_{\boldsymbol{C}\boldsymbol{C}}\Psi_{\text{ani}}(\boldsymbol{C},\boldsymbol{A}_1,\boldsymbol{A}_2) \tag{26}$$

The directional stiffness (DS) can be defined as

$$\text{DS} := \boldsymbol{n}\otimes\boldsymbol{n} : \mathbb{C}_{\text{ani}} : \boldsymbol{n}\otimes\boldsymbol{n} \quad \text{with} \quad \boldsymbol{n} = \cos\alpha\boldsymbol{e}_1 + \sin\alpha\boldsymbol{e}_2, \quad \alpha\in[0,2\pi]\,. \tag{27}$$

---

[2] It is not common to use second invariant I_2 in modeling isotropic response of soft biological tissues. For this, we omitted the stress terms resulting from dependency of free-energy function on I_2 .

[3] Herein, M_{ji} and m_{ji} corresponds to the ith components of the fiber orientation vectors $\boldsymbol{M}_i$

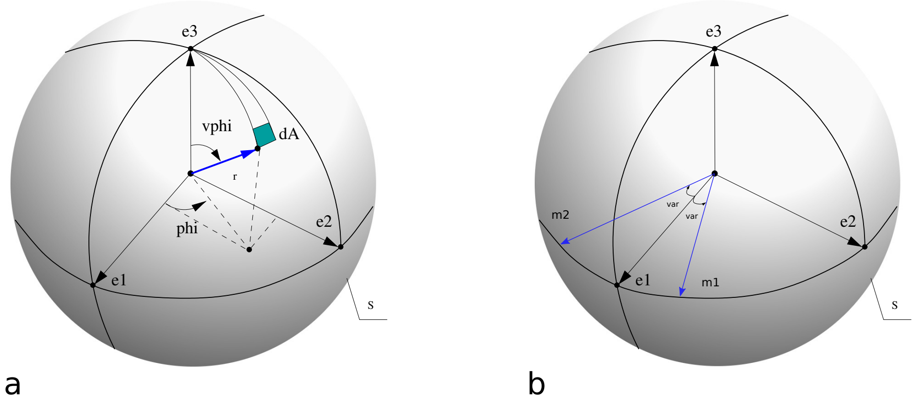

Fig. 3 (a) The unit micro-sphere and the orientation vector, (b) mean fiber directions of two families of fiber lie on $\boldsymbol{e}_1$-$\boldsymbol{e}_2$ plane.

2.2.2 Dispersion-type anisotropic formulations

The tissue is considered a fiber-reinforced composite with the fibers distributed within an isotropic matrix in the dispersion-type anisotropic formulation; the models developed within this framework accurately describe the effect of the structural arrangement of the fibers on the mechanical response. Dispersion-type anisotropic approaches utilize density distribution functions to represent the distributed fiber architecture of tissues. Let unit fiber direction $\boldsymbol{r}$ on a unit-sphere be given in the undeformed configuration. The fiber density in direction $\boldsymbol{r}$ is expressed with $\rho(\boldsymbol{r})$. The unit fiber orientation vector can be expressed in spherical coordinates as follows

$$\boldsymbol{r} = \sin\theta\cos\phi\boldsymbol{e}_1 + \sin\theta\sin\phi\boldsymbol{e}_2 + \cos\theta\boldsymbol{e}_3\,, \tag{28}$$

in terms of Eulerian angles $\theta \in [0, \pi]$ and $\phi \in [0, 2\pi]$, see Figure 3. The Eulerian counterpart of $\boldsymbol{r}$ is derived as $\boldsymbol{t} = \boldsymbol{F}\boldsymbol{r}$. In this part, we will summarize the two kinematic approaches for the modeling of dispersion-type anisotropy in soft biological tissues.

(i) Generalized structure tensor (GST) formulations: The generalized structure tensor is defined as

$$\mathbf{H} = \frac{1}{\mid \mathscr{S} \mid} \int_{\mathscr{S}} \rho(\boldsymbol{r})\boldsymbol{r} \otimes \boldsymbol{r}\, dA \quad \text{with} \quad \operatorname{tr}\mathbf{H} = 1\,, \tag{29}$$

and $\mid \mathscr{S} \mid = 4\pi$ for a unit sphere. Let $\boldsymbol{h} = \boldsymbol{F}\boldsymbol{H}\boldsymbol{F}^T$ be defined as the Eulerian counterpart of the generalized structure tensor. The Lagrangian and Eulerian stresses can be obtained by applying the chain rule

$$\boldsymbol{S} = 2\partial_{\boldsymbol{C}}\psi = 2\left[\frac{\partial U}{\partial J}\frac{\partial J}{\partial \boldsymbol{C}} + \frac{\partial \Psi_{\text{iso}}}{\partial I_1}\frac{\partial I_1}{\partial \boldsymbol{C}} + \frac{\partial \Psi_{\text{ani}}}{\partial E}\frac{\partial E}{\partial \boldsymbol{C}}\right], \tag{30}$$

where

$$E := \boldsymbol{H} : \boldsymbol{C} - 1 \qquad \text{or} \qquad E := \boldsymbol{h} : \boldsymbol{1} - 1 \tag{31}$$

is the one-dimensional mean anisotropic fiber strain akin to the Green-Lagrangian strain. The closed form expressions for the Lagrangian and Eulerian stress tensors require the following derivatives

$$\boldsymbol{S} = 2\psi_1\boldsymbol{1} + 2\psi_f\boldsymbol{H} - p\boldsymbol{C}^{-1} \quad \text{and} \quad \boldsymbol{\tau} = 2\psi_1\boldsymbol{b} + 2\psi_f\boldsymbol{h} - p\boldsymbol{1} \tag{32}$$

with $\psi_f = \partial_E \Psi_{\text{ani}}$. In the principal directions, (32) can be written in terms of the principal stretches,

$$S_i = 2\psi_1 + 2\psi_f H_i - \frac{1}{\lambda_i^2} p \quad \text{and} \quad \tau_i = 2\psi_1 \lambda_i^2 + 2\psi_f h_i - p\,. \tag{33}$$

The anisotropic part of the Lagrangian moduli expression can be written as

$$\mathbb{C}_{\text{ani}} = 4\frac{\partial^2 \psi}{\partial \boldsymbol{C}^2} = 4\psi_{ff} \boldsymbol{H}_1 \otimes \boldsymbol{H}_1 + 4\psi_{ff} \boldsymbol{H}_2 \otimes \boldsymbol{H}_2 \quad \text{with} \quad \psi_{ff} = \frac{\partial^2 \Psi_{\text{ani}}}{\partial E^2}\,. \tag{34}$$

(ii) Angular integration (AI) formulations: The total free-energy of fibers is calculated by

$$\Psi_{\text{ani}} = \frac{1}{\mid \mathscr{S} \mid} \int_{\mid \mathscr{S} \mid} \rho(\boldsymbol{r}) \psi_{fib}(\lambda_f)\, dA \quad \text{where} \quad \lambda_f = |\boldsymbol{F}\boldsymbol{r}|\,, \tag{35}$$

and $\mathscr{S}$ represents a unit sphere with $\mid \mathscr{S} \mid = 4\pi$. ψ_{fib} is the contribution to the free energy function in each orientation direction $\boldsymbol{r}$. Moreover, let $\boldsymbol{t} = \boldsymbol{F}\boldsymbol{r}$ denote the orientation vector $\boldsymbol{r}$ in the deformed configuration. Starting with the free-energy (35), the Eulerian stress tensor follows by the application of the chain rule

$$\boldsymbol{\tau} = J\frac{\partial \Psi_{\text{iso}}}{\partial J}\boldsymbol{1} + 2\frac{\partial \Psi_{\text{iso}}}{\partial I_1}\boldsymbol{b} + \int_{\mathscr{S}} \rho(\boldsymbol{r}) \lambda_f^{-1} \frac{\partial \psi_{fib}}{\partial \lambda_f} \boldsymbol{t} \otimes \boldsymbol{t}\, dA\,. \tag{36}$$

Then, the Kirchhoff stress expression reads

$$\boldsymbol{\tau} = -p\boldsymbol{1} + 2\psi_1 \boldsymbol{b} + \int_{\mathscr{S}} \rho(\boldsymbol{r}) \lambda_f^{-1} \psi_f \boldsymbol{t} \otimes \boldsymbol{t}\, dA \tag{37}$$

with $\tilde{\psi}_f = \partial_{\lambda_f} \psi_{fib}$. Insertion of (28) into (37) and for $\boldsymbol{F} = \text{diag}[\lambda_1, \lambda_2, \lambda_3]$, the Kirchhoff stresses in principal directions can be written as

$$\begin{aligned}
\tau_1 &= -p + 2\psi_1 \lambda_1^2 + \lambda_1^2 \int_{\mathscr{S}} \rho(\boldsymbol{r}) \lambda_f^{-1} \tilde{\psi}_f \cos^2\phi \, \sin^2\theta \, dA\,, \\
\tau_2 &= -p + 2\psi_1 \lambda_2^2 + \lambda_2^2 \int_{\mathscr{S}} \rho(\boldsymbol{r}) \lambda_f^{-1} \tilde{\psi}_f \sin^2\phi \, \sin^2\theta \, dA\,, \\
\tau_3 &= -p + 2\psi_1 \lambda_3^2 + \lambda_3^2 \int_{\mathscr{S}} \rho(\boldsymbol{r}) \lambda_f^{-1} \tilde{\psi}_f \cos^2\theta \;\; dA\,,
\end{aligned} \tag{38}$$

where $dA = \sin\theta d\theta d\phi$, see Figure 3.

2.3 Stresses under homogeneous deformations

In this section, we briefly outline the deformation state of anisotropic biological tissues subjected to uniaxial and equibiaxial stresses. Under macroscopic stress states such as uniaxial or biaxial tension, the deformation gradient of anisotropic materials cannot be expressed in a straightforward manner as is the case for incompressible isotropic materials. This is due to induced shear deformation that compensate the stress contribution of fibers having an orientation different from the principal stress

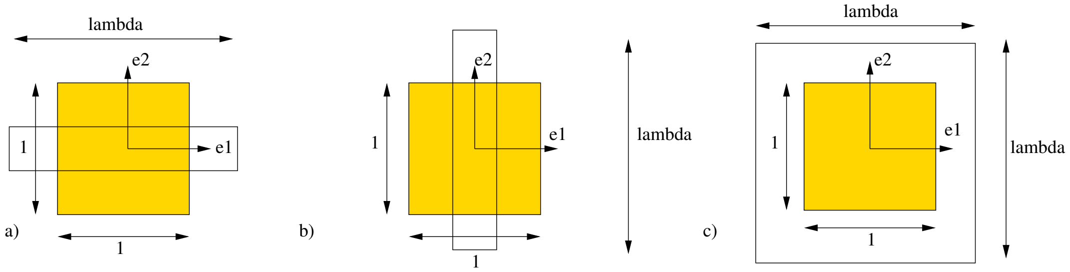

Fig. 4 Deformation modes: (a) uniaxial tension in $\boldsymbol{e}_1$ direction along with the mean fiber direction $\boldsymbol{M}_1$, (b) uniaxial tension in $\boldsymbol{e}_2$ along with the transverse direction of mean fiber direction $\boldsymbol{M}_1$, and (c) equibiaxial tension in $\boldsymbol{e}_1$-$\boldsymbol{e}_2$ plane with the mean fiber directions $\boldsymbol{M}_1$, $\boldsymbol{M}_2$ symmetrical around $\boldsymbol{e}_1$ direction.

axes. Therefore, the components of the deformation gradient should be obtained iteratively to satisfy equilibrium conditions, e.g. in the case of uniaxial tension $\sigma_{22} = \sigma_{33} = \sigma_{12} = \sigma_{13} = \sigma_{23} = 0$ and $\sigma_1 = \hat{\sigma}_{app}$. Exception occurs when the applied stress/deformation(s) coincide(s) with the material symmetry axes. To this end, we assume that the material is deformed in the principal directions corresponding to the principal axes of fiber orientations for AI- or GST-based models. For invariant formulations, the deformation axes are assumed to coincide with the symmetry axes for the two fiber family formulations, while in single fiber family formulations one of the principal deformation axes coincides with the fiber direction. Such an ansatz avoids *a priori* shear strains/stresses, leading to diagonal deformation and stress tensors. In this context, the deformation gradient and the nominal stress expression under homogeneous uniaxial, equibiaxial or pure shear deformations can be expressed as follows

$$\boldsymbol{F} = \begin{bmatrix} F_{11} & 0 & 0 \\ 0 & F_{22} & 0 \\ 0 & 0 & F_{33} \end{bmatrix} \quad \text{and} \quad \boldsymbol{P} = \begin{bmatrix} P_1 & 0 & 0 \\ 0 & P_2 & 0 \\ 0 & 0 & P_3 \end{bmatrix} . \tag{39}$$

Uniaxial tension: For an incompressible anisotropic hyperelastic solid, the deformation and stress states under uniaxial tension are

$$\boldsymbol{F} = \begin{bmatrix} \lambda & 0 & 0 \\ 0 & \frac{1}{\sqrt{\lambda}} & 0 \\ 0 & 0 & \frac{1}{\sqrt{\lambda}} \end{bmatrix} \quad \text{and} \quad \boldsymbol{P} = \begin{bmatrix} P_1 & 0 & 0 \\ 0 & 0 & 0 \\ 0 & 0 & 0 \end{bmatrix} , \tag{40}$$

see Figure 4(a-b). It is important to note that (40) holds for isotropic elasticity and transverse isotropy with $\boldsymbol{M}_1 = \boldsymbol{e}_1$. Due to the the imposition of tension only condition, (40) is also valid for $\boldsymbol{M}_1 = \boldsymbol{e}_2$ or $\boldsymbol{M}_1 = \boldsymbol{e}_3$. The first two invariants under uniaxial deformation read

$$I_1 = \lambda^2 + \frac{2}{\lambda} \quad \text{and} \quad I_2 = 2\lambda + \frac{1}{\lambda^2} . \tag{41}$$

For symmetrically orthotropic fibers, the equalities $I_4 = I_6$ and $I_5 = I_7$ hold leading to

$$I_4 = I_6 = \lambda^2 \cos^2\varphi + \frac{1}{\lambda} \sin^2\varphi \quad \text{and} \quad I_5 = I_7 = \lambda^4 \cos^2\varphi + \frac{1}{\lambda^2} \sin^2\varphi , \tag{42}$$

where φ is the angle between the fiber and the symmetry axis $\boldsymbol{e}_1$. The components of the nominal stresses under uniaxial loading in the symmetry axes for the invariant-, generalized structure tensor- and angular integration-based formulations read

$$\boxed{\begin{aligned} \text{Inv}: P_1 &= 2\psi_1\lambda + 2\psi_4 M_{11}^2\lambda + 4\psi_5 M_{11}^2\lambda^3 + 2\psi_6 M_{21}^2\lambda + 4\psi_7 M_{21}^2\lambda^3 - \frac{1}{\lambda}p \\ \text{GST}: P_1 &= 2\psi_1\lambda + 2\psi_f' H_1\lambda - \frac{1}{\lambda}p \\ \text{AI}: P_1 &= n\lambda \textstyle\int_{\mathscr{S}} \rho(\boldsymbol{r})\lambda_f^{-1}\tilde{\psi}_f \cos^2\phi \sin^3\theta \, dA + 2\psi_1\lambda - \frac{1}{\lambda}p \end{aligned}} \tag{43}$$

Equibiaxial tension: For an incompressible hyperelastic anisotropic solid, the deformation and stress states under equibiaxial tension are

$$\boldsymbol{F} = \begin{bmatrix} \lambda & 0 & 0 \\ 0 & \lambda & 0 \\ 0 & 0 & \lambda^{-2} \end{bmatrix} \quad \text{and} \quad \boldsymbol{P} = \begin{bmatrix} P_1 & 0 & 0 \\ 0 & P_2 & 0 \\ 0 & 0 & 0 \end{bmatrix}. \tag{44}$$

see Figure 4(c). The first two invariants under equibiaxial deformation read

$$I_1 = 2\lambda^2 + \frac{1}{\lambda^4}\,, \quad I_2 = \lambda^4 + \frac{2}{\lambda^2}\,. \tag{45}$$

The invariants associated with the structural tensors are

$$I_4 = I_6 = \lambda^2\cos^2\varphi + \lambda^2\sin^2\varphi \quad \text{and} \quad I_5 = I_7 = \lambda^4\cos^2\varphi + \lambda^4\sin^2\varphi\,. \tag{46}$$

The components of the nominal stresses under equibiaxial loading in the symmetry axes for invariant-, generalized structure tensor- and angular integration-based formulations read

$$\boxed{\begin{aligned} \text{Inv}: P_1 &= 2\psi_1\lambda + 2\psi_4 M_{11}^2\lambda + 4\psi_5 M_{11}^2\lambda^3 + 2\psi_6 M_{21}^2\lambda + 4\psi_7 M_{21}^2\lambda^3 - \frac{1}{\lambda}p \\ P_2 &= 2\psi_1\lambda + 2\psi_4 M_{12}^2\lambda + 4\psi_5 M_{12}^2\lambda^3 + 2\psi_6 M_{22}^2\lambda + 4\psi_7 M_{22}^2\lambda^3 - \frac{1}{\lambda}p \\ \text{GST}: P_1 &= 2\psi_1\lambda + 2\psi_f' H_1\lambda - \frac{1}{\lambda}p \\ P_2 &= 2\psi_1\lambda + 2\psi_f' H_2\lambda - \frac{1}{\lambda}p \\ \text{AI}: P_1 &= n\lambda \textstyle\int_{\mathscr{S}} \rho(\boldsymbol{r})\lambda_f^{-1}\tilde{\psi}_f \cos^2\phi \sin^3\theta \mathrm{d}\theta \mathrm{d}\phi + 2\psi_1\lambda - \frac{1}{\lambda}p \\ P_2 &= n\lambda \textstyle\int_{\mathscr{S}} \rho(\boldsymbol{r})\lambda_f^{-1}\tilde{\psi}_f \sin^2\phi \sin^3\theta \, dA + 2\psi_1\lambda - \frac{1}{\lambda}p\,. \end{aligned}} \tag{47}$$

3 Anisotropic hyperelastic material models

In this section, we will review the Neo-Hooekan isotropic constitutive model and 12 anisotropic hyperelastic models under two main categories: (i) strain invariant-based models, and (ii) fiber dispersion-based models.[4]. There exist many more models in

---

[4] Dispersion-type anisotropic models may as well include invariant terms for the description of isotropic matrix. Here, we focus on the representation of the anisotropic response dominated by the collagen fiber distribution

Table 1 Summary of the constitutive models used for the numerical investigation

#	model	type	Isotropic/Anisotropic part	developed/calibrated for
1	NY model	I_1, I_4	–/ Fung-type	mitral valve
2	HGO model	I_1, I_4	Neo-Hookean/Fung-type	arterial wall
3	HSGR model	I_1, I_4	Neo-Hookean/Fung-type	arterial wall
4	OS model	I_1, I_4	Neo-Hookean/Fung-type	arterial wall
5	HY model	I_1, I_4	Fung- / Fung-type	cardiac tissue
6	GOH model	GST	Neo-Hookean/Fung-type exponential	arterial wall
7	HNORS model	GST	Neo-Hookean/Fung-type exponential	arterial wall
8	AMDM model	AI	Neo-Hookean/Fung-type exponential	arterial wall
9	ASMD model	AI	Neo-Hookean/Fung-type exponential	arterial wall
10	DBB model	AI	Neo-Hookean/Fung-type exponential	art. wall/aortic valve
11	LOH model	AI	Neo-Hookean/ Fung-type exponential	arterial wall
12	ARCCH model	AI	–/ Power type	articular cartilage

the literature as outlined in the Introduction. An *in silico* based review of all existing models is not feasible due to the constraints of time and resources. Therefore we confine ourselves to a limited number of models. During the selection process, the free-energy functions of Fung-type (an)isotropic models and Neo-Hooke type isotropic free-energy functions are preferred due to their apparent success relative to other phenomenological forms. In order to compare the performance of free-energy functions that are borrowed from non-Gaussian rubber elasticity and power-type free-energy functions relative to the Fung-type (an)isotropic forms, the model of Ogden and Saccomandi [80], and the model of Ateshian et al. [4] are included in the investigation. Due to the recent trends/developments in the dispersion-type hyperelasticity, we included various forms of dispersion models and focused on their performance relative to their invariant counterparts. For this purpose, the free-energy functions of the selected models are mostly identical. They differ from one another with regard to the kinematic assumptions involved in the mathematical description. All the models that are investigated are briefly outlined in Table 1. We pursue our investigation as follows: The free-energy functions and necessary derivatives for the stress expressions are outlined. In order to emphasize the degree of anisotropy and the anisotropy distribution obtained from parameter identification process from each tissue is presented in terms of polar plots for each constitutive model investigated. The polar plots consider the density distribution (DD) function for the plane of interest along with the directional stiffness (DS) computed from equation (27). In the case of invariant formulations, the density distribution can be represented by a Dirac delta function. In order to get more insight into the anisotropic mechanical response of invariant-based formulations, an alternative indicator, the directional stiffness is utilized and compared to those obtained from dispersion-type formulations. To this end, the polar plots of the directional stiffness obtained merely from the anisotropic part of the initial elastic moduli tensor is used for visualization of the plane of interest.

3.1 Invariant-based models

3.1.1 The Neo-Hookean model

The invariant-based models assume perfect alignment of fibers embedded into an isotropic ground matrix. Models have been presented for two families of fibers symmetrically disposed. The Neo-Hookean model is the most fundamental hyperelastic constitutive model. Many researchers represent the isotropic ground matrix of soft tissues with the Neo-Hookean model [1, 2, 44, 50, 94]. Therefore, it deserves a separate description. Based on Wall's treatment of elasticity of a molecular network, Treloar [90] proposed the following free-energy function

$$\Psi_{\text{iso}} = \frac{1}{2} n k_B \theta \left(\lambda_1^2 + \lambda_2^2 + \lambda_3^2 - 3\right) \quad \text{or} \quad \Psi_{\text{iso}} = \frac{1}{2}\mu\left(I_1 - 3\right) \tag{48}$$

with $\mu = n k_B \theta$. Herein, n is the volume specific chain density, k_B is the Boltzmann constant and θ is the absolute temperature, and $\mu = n k_B \theta$ is the shear modulus. The non-zero derivative of ψ with respect to the invariants is

$$\psi_1 = \frac{\mu}{2} \ . \tag{49}$$

3.1.2 Newman-Yin (NY) model

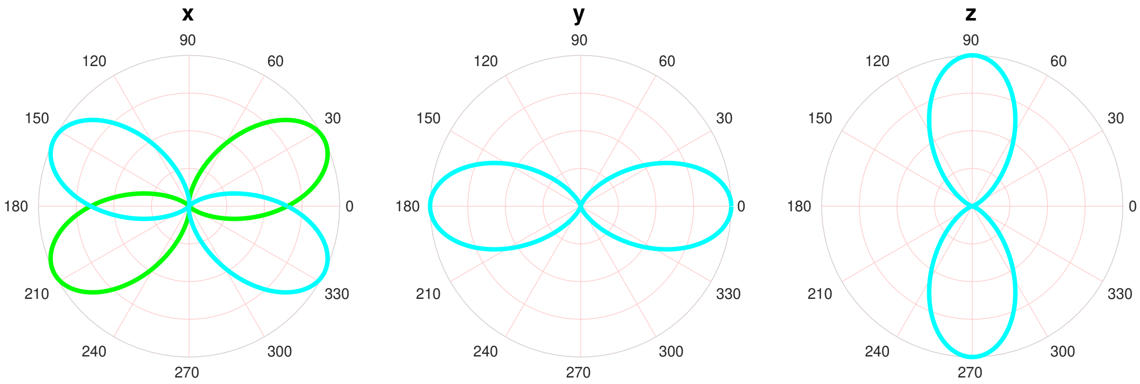

Fig. 5 The polar plots of the directional stiffness (DS) for invariant based NY model [71], HGO model [44], HSGR model [50], OS model [80], and HY model [56]: (a) two families of fibers distribution based on ET dataset for AAA tissue [79], (b) one family of fibers distribution based on UT dataset for the linea alba [19], (c) one family of fibers distribution based on UT dataset for the rectus sheath [70].

Newman and Yin [71] proposed an exponential free-energy form analogous to the one proposed by Fung et al. [31] to describe hyperelastic behavior of mitral valve tissue.The mitral valve is an important structural element of the heart. The collagen fibers inside the mitral valve are relatively uniform through the thickness and within the experimental test region as reported in [71]. Based on these facts, Newman and Yin [71] assumed that the material is transversely isotropic and that the free-energy function depends on the first and the fourth invariants, like all other models of one family of fibers. They observed that for a constant I_4, both ψ_1 and ψ_4 increase nonlinearly. Therefore, they proposed,

$$\Psi_{\text{ani}} = k_0(\exp(Q) - 1) \quad \text{with} \quad Q = (k_1(I_1 - 3)^2 + k_2(\sqrt{I_4} - 1)^4) + k_2(\sqrt{I_6} - 1)^4) \ . \tag{50}$$

Q is the quadratic function of the invariants. In order to have a strain energy increases with increasing I_4, k_0 should be positive. Also, if the tissue is not able to support compressive load, k_2 should be positive. The original model was proposed for tissues with a single family of fibers. In this work, we have extended the formulation considering two families of fibers as given in $(50)_2$ by incorporating the latter term depending on I_6. The derivatives of Ψ_{ani} with respect to the invariants are

$$\begin{aligned} \psi_1 &= 2k_0k_1(I_1-3)\exp(Q)\,, \quad \psi_4 = 2k_0k_2\exp(Q)\frac{1}{\sqrt{I_4}}(\sqrt{I_4}-1)^3\,, \\ \psi_6 &= 2k_0k_2\exp(Q)\frac{1}{\sqrt{I_6}}(\sqrt{I_6}-1)^3\,. \end{aligned} \tag{51}$$

The polar plots of the directional stiffness for the NY model obtained with the identified parameters for each tissue are depicted in Figure 5.

3.1.3 Holzapfel-Gasser-Ogden (HGO) model

Holzapfel et al. [44] proposed a constitutive model for arteries. Arterial walls are composed of three distinct layers; innermost layer the intima, middle layer the media, and outermost layer the adventitia. Holzapfel et al. considered each layer of the artery as a fiber-reinforced composite by incorporating histological information such as fiber directions. They additively decomposed the isochoric free-energy function into isotropic and anisotropic parts,

$$\Psi = \Psi_{\text{iso}}(I_1) + \Psi_{\text{ani}}(I_4, I_6)\,. \tag{52}$$

They utilized the Neo-Hookean model (48) for the isotropic part since collagen fibers are thought to not contribute to the mechanical behavior of the tissue at low pressures. The free-energy stored by two families of collagen fibers is described as

$$\Psi_{\text{ani}}(I_4, I_6) = \frac{k_1}{2k_2}\sum_{i=4,6}\left(\exp[k_2\langle I_i-1\rangle^2]-1\right) \tag{53}$$

where $k_1 > 0$ is a stress-like parameter and $k_2 > 0$ is a dimensionless parameter. The collagen fibers do not support compressive stresses due to their wavy nature. Therefore, the Macauley brackets $\langle(\bullet)\rangle = [(\bullet)+|(\bullet)|]/2$ are utilized in order to filter out the tensile stretches. The derivatives of ψ_i with respect to the i^{th} invariants are

$$\psi_4 = k_1\langle I_4-1\rangle\exp\left(k_2\langle I_4-1\rangle^2-1\right)\,, \quad \psi_6 = k_1\langle I_6-1\rangle\exp\left(k_2\langle I_6-1\rangle^2-1\right)\,. \tag{54}$$

The polar plots of the directional stiffness for the HGO model obtained with the identified parameters for each tissue are depicted in Figure 5.

3.1.4 Holzapfel-Sommer-Gasser-Regitnig (HSGR) model

Holzapfel et al. [50] proposed a free-energy function of the form $\Psi(I_1, I_4) = \Psi_{\text{iso}}(I_1) + \Psi_{\text{ani}}(I_1, I_4)$. The model uses the Neo-Hookean model (48) as the isotropic part of the free-energy function. The anisotropic part of the free-energy function has a mixed representation

$$\Psi_{\text{ani}} = \text{sgn}\langle I_4-1\rangle\frac{k_1}{k_2}\left(\exp\{k_2[(1-p)(I_1-3)^2+p\langle I_4-1\rangle^2]\}-1\right)\,, \tag{55}$$

where $k_1 > 0$ is a stress-like parameter and $k_2 >$ is a dimensionless parameter. The measure of anisotropy parameter $p \in [0,1]$ interpolates between the contributions of the first I_1 and fourth invariants I_4. It mimics the degree of fiber dispersion phenomenologically. The switch function $\text{sgn}\langle I_4-1\rangle$ enforces the tension-only condition and is activated for $I_4 - 1 > 0$. The model recovers the HGO model for $p = 1$. The fiber related terms drop and the model reduces to an exponential isotropic model for $p = 0$. The non-zero derivatives of the free-energy function are

$$\begin{aligned} \psi_1 &= \frac{\mu}{2} + 2k_1(1-p)(I_1-3)\mathrm{sgn}\langle I_4 - 1\rangle \exp\{k_2[(1-p)(I_1-3)^2 + p\langle I_4 - 1\rangle^2]\}\,, \\ \psi_4 &= 2\frac{k_1}{k_2} p\langle I_4 - 1\rangle \exp\{k_2[(1-p)(I_1-3)^2 + p\langle I_4 - 1\rangle^2]\}\ . \end{aligned} \tag{56}$$

This model was originally proposed for coronary arteries with nonatherosclerotic intimal thickening.

3.1.5 Ogden-Saccomandi (OS) model

Ogden and Saccomandi [80], following the work of Horgan and Saccomandi [52], proposed a logarithmic constitutive law for arterial tissue with two fiber families in which the fiber extension is limited. They additively decomposed the free-energy function into isotropic and anisotropic parts,

$$\Psi = \Psi_{\text{iso}}(I_1) + \Psi_{\text{ani}}(I_4, I_6)\,. \tag{57}$$

To model the isotropic behavior of the tissue, they adapted the well-known rubber elasticity model of Gent [35]. The free-energy function of the Gent model reads

$$\Psi_{\text{iso}} = -\frac{1}{2}\mu J_m \ln\left(1 - \frac{I_1 - 3}{J_m}\right)\,, \tag{58}$$

where μ is the shear modulus and J_m is the parameter that controls the chain extensibility limit for the matrix material. The deformation limit for the first invariant is $I_1 < 3 + J_m$ and the stresses tend to infinity asymptotically at this limit. As $J_m \to \infty$, the isotropic part of the free-energy function (58) recovers the Neo-Hookean model. A similar model of Gent [35] was proposed by Horgan and Saccomandi [52] for transversely isotropic materials. Instead of limiting the polymer chain extensibility, the model of Horgan and Saccomandi limits the extensibility of the fibers. The anisotropic part of the free-energy function is

$$\Psi_{\text{ani}} = -\frac{k_1}{2} J_f \sum_{\alpha=4,6} \ln\left(1 - \frac{\langle I_\alpha - 1\rangle^2}{J_f}\right)\,, \tag{59}$$

where k_1 is a stress-like parameter, and J_f is the limiting parameter of extensibility of collagen fibers. The constraint

$$I_\alpha < \sqrt{J_f} + 1\,, \quad \{\alpha{=}4{,}6\}\,. \tag{60}$$

confines the stretches beyond the fiber extensibility limit. The derivatives of the free-energy function are

$$\psi_1 = \frac{\mu}{2}\left(\frac{J_m}{J_m - I_1 + 3}\right)\,, \quad \psi_\alpha = k_1 J_f\left(\frac{\langle I_\alpha - 1\rangle}{J_f - \langle I_\alpha - 1\rangle^2}\right)\,, \quad \{\alpha{=}4{,}6\} \tag{61}$$

The polar plots of the directional stiffness for the OS model obtained with the identified parameters for each tissue are depicted in Figure 5.

3.2 Humphrey and Yin (HY) model

Humphrey & Yin [56] proposed a model to capture the passive response of cardiac tissue. They additively decomposed the free-energy function into isotropic and anisotropic parts. The isotropic part's free-energy function was responsible to represent the behavior of non-muscular constituents of the tissue, whereas the anisotropic part is responsible for muscle fibers. For the isotropic part, they adopted the model proposed by Demiray [23]

$$\Psi_{\text{iso}} = c[\exp(b(I_1 - 3)) - 1] \tag{62}$$

and for the anisotropic part, an exponential function in terms of the square root of the fourth invariant was employed

$$\Psi_{\text{ani}} = A[\exp(b(\sqrt{I_4} - 1)) - 1] \tag{63}$$

The derivatives of the free-energy function are

$$\begin{aligned} \psi_1 &= c\ b\ \exp(b(I_1 - 3))\,, \\ \psi_4 &= A\ a(\sqrt{I_4} - 1)\exp(a(\sqrt{I_4} - 1)^2)/\sqrt{I_4}\ . \end{aligned} \tag{64}$$

The polar plots of the directional stiffness for the HY model obtained with the identified parameters for each tissue are depicted in Figure 5.

3.3 Dispersion-type anisotropic constitutive models

It has been determined that not only do the mean orientation of fibers within soft tissues affect their mechanical properties, but also the amount by which they are dispersed around the mean [49]. For instance, if the majority of fibers are orientated along the direction of the mean, the behavior will be very different to that if the fibers are distributed in a cone-like span around the mean orientation [34]. For this reason, a number of models have been developed to incorporate dispersion into the constitutive law describing the stress-strain relation of the tissue. These fiber dispersion-based models utilize a probability distribution function to model the histological structure of tissues. The models which have an angular integration approach and a generalized structure tensor approach are outlined in this section.

3.3.1 GST-based Gasser-Ogden-Holzapfel (GOH) model

Gasser et al. [34] assumed that the tissue's fibers are distributed rotationally symmetric around a mean fiber orientation direction $\boldsymbol{M}$. They utilized a planar π-periodic von-Mises distribution as a fiber density distribution around $\boldsymbol{M}$. The von-Mises distribution function is a one-dimensional probability distribution which is a function of Θ and concentration parameter b. The standard von-Mises distribution function is

$$\bar{\rho}(\Theta) = \frac{\exp[b(\cos(2\Theta))}{2\pi I_0(b)} \quad \text{with} \quad I_0(b) = \frac{1}{\pi}\int_0^{\pi} \exp(b\cos\Theta)\mathrm{d}\Theta\,, \tag{65}$$

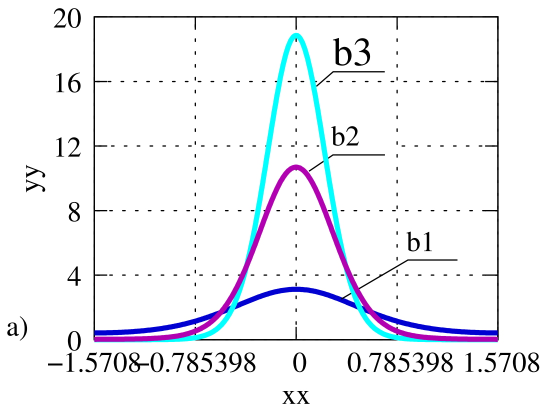

Fig. 6 (a) Graphical representation of the von-Mises distribution of collagen fibers and (b) relation between the dispersion parameter κ and the concentration parameter of the von-Mises distribution.

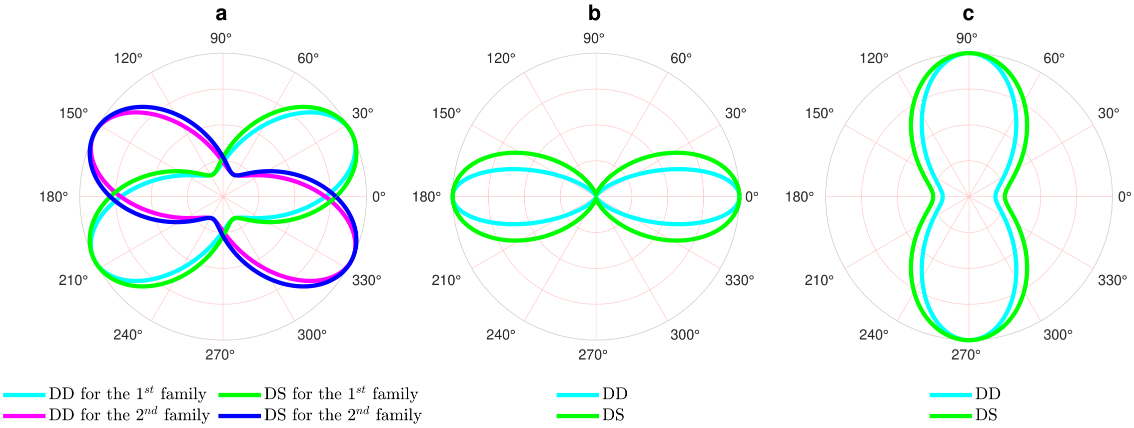

Fig. 7 The polar plots of the density distribution (DD) and the directional stiffnesses (DS) for the GOH model [34]: (a) two families of fibers distribution based on ET dataset for AAA tissue [79], (b) one family of fibers distribution based on UT dataset for the linea alba [19], (c) one family of fibers distribution based on UT dataset for the rectus sheath [70].

where $I_0(b)$ is a modified Bessel function of the first kind of order zero. Applying the normalization condition to (65) gives the relation

$$I \equiv \int_0^\pi \bar{\rho}(\Theta)\sin\Theta \mathrm{d}\Theta \equiv \frac{\exp(-b)}{2\sqrt{2\pi b}}\frac{\mathrm{erfi}(\sqrt{2b})}{I_0(b)}\,. \tag{66}$$

The normalized von-Mises distribution is

$$\rho(\Theta) = \frac{\bar{\rho}(\Theta)}{I} = 4\sqrt{\frac{b}{4\pi}}\frac{\exp\left(b\cos(2\Theta)+1\right)}{\mathrm{erfi}\sqrt{2b}}\,. \tag{67}$$

By inserting the von-Mises type density distribution function (67) into (29), the generalized structure tensor can be written as

$$\boldsymbol{H} = \kappa\mathbf{1} + (1-3\kappa)\boldsymbol{M}\otimes\boldsymbol{M} \quad \text{where} \quad \kappa = \frac{1}{4}\int_0^\pi \rho(\Theta)\sin^3\Theta \mathrm{d}\Theta \tag{68}$$

is the fiber dispersion parameter. A one-to-one relation exists between the dispersion parameter κ and the concentration parameter b, see Figure 6. Hence, $\kappa \in [0, 1/3]$ enters the constitutive model as an additional material parameter responsible for the

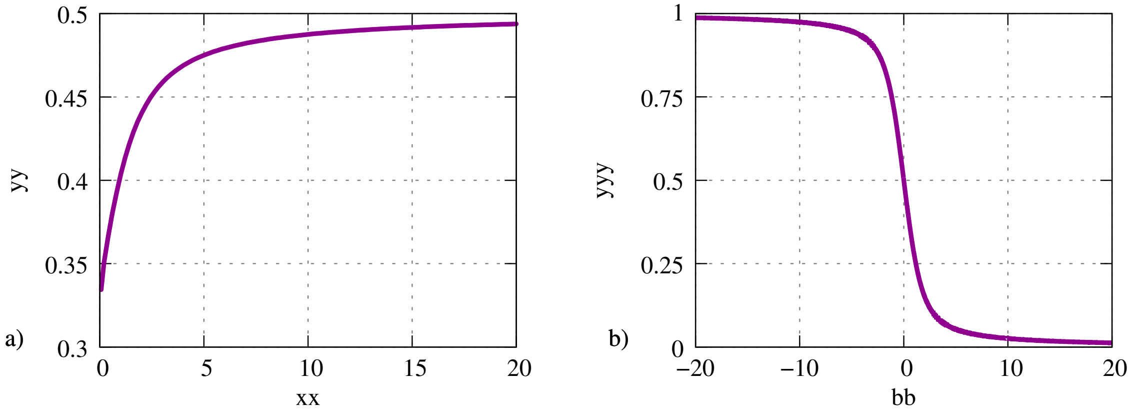

Fig. 8 (a) Relation between the dispersion parameter κ_{op} and the out-of-plane concentration parameter b of von-Mises distribution and (b) relation between the dispersion parameter κ_{ip} and the in-plane concentration parameter a of von-Mises distribution.

degree of dispersion. The lower limit $\kappa = 0$ recovers the invariant-based anisotropy and the upper limit $\kappa = 1/3$ leads to an isotropic constitutive response. The polar plots of the density distribution and directional stiffness for the GOH model obtained with the identified parameters for each tissue are depicted in Figure 7. Gasser et al. [34] can be considered as the GST counterpart of the GHO model [44]. The anisotropic part of the free-energy function reads

$$\Psi_{\text{ani}}(\boldsymbol{C}, \boldsymbol{H}_i) = \frac{k_1}{2k_2}[\exp(k_2 E_i^2) - 1]\,, \quad i = 1, 2 \tag{69}$$

where $E_i = \boldsymbol{H}_i : \boldsymbol{C} - 1$ replaces the fourth and sixth invariants in the GHO model. The classical Neo-Hookean model (48) is utilized for the isotropic part of the free-energy function. The derivative of the anisotropic free-energy function with respect to the mean fiber strain reads

$$\psi_{fib} = k_1 E_i \exp(k_2 E_i^2)\,. \tag{70}$$

3.3.2 GST-based Holzapfel-Niestrawska-Ogden-Reinisch-Schriefl (HNORS) model

Holzapfel et al. [46] take into account both the in- and out-of-plane dispersion of fibers based on the observations of Schriefl et al. [84, 85] where they recorded that the fibers are dispersed both in-plane and out-of-plane in arterial walls. Their observations reveal that no correlation exists between in- and out-of-plane dispersions. Based on these arguments, the probability density function is multiplicatively decomposed as

$$\rho(\boldsymbol{r}) = \rho_{ip}(\Phi)\rho_{op}(\Theta). \tag{71}$$

For in-plane distribution, they considered a basic von-Mises distribution

$$\rho_{ip}(\Phi) = \frac{\exp[a(\cos(2\Theta))}{I_0(a)} \quad \text{with} \quad I_0(a) = \frac{1}{\pi}\int_0^{\pi} \exp(x\cos\alpha)d\alpha \tag{72}$$

where a is the concentration parameter and $I_0(a)$ is the modified Bessel function of the first kind of order zero. The out-of-plane distribution is in the form

$$\rho_{op}(\Theta) = 2\sqrt{\frac{2b}{\pi}}\frac{\exp[b(\cos(2\Theta)) - 1]}{\mathrm{erf}(\sqrt{2b})} \ . \tag{73}$$

The measures of dispersion in the in-plane and the out-of-plane directions read

$$\kappa_{ip} = \frac{1}{\pi}\int_0^{\pi} \rho_{ip}(\Phi)\sin^2\Phi \mathrm{d}\Phi \quad \text{and} \quad \kappa_{op} = \int_0^{\pi/2} \rho(\Theta)\sin^3\Theta \mathrm{d}\Theta \tag{74}$$

The structure tensor $\boldsymbol{H}$ has the form

$$\boldsymbol{H} = 2\kappa_{ip}\kappa_{op}\mathbf{1} + 2\kappa_{op}(1 - 2\kappa_{ip})\boldsymbol{M}_i \otimes \boldsymbol{M}_i + (1 - 2\kappa_{op} - 2\kappa_{ip}\kappa_{op})\boldsymbol{M}_n \otimes \boldsymbol{M}_n \tag{75}$$

where $\boldsymbol{M}_i$ is the in-plane mean fiber direction, whereas $\mathbf{M}_n$ is the out-of-plane vector. The Eulerian counterpart of the generalized structure tensor reads

$$\boldsymbol{h} = 2\kappa_{ip}\kappa_{op}\mathbf{1} + 2\kappa_{op}(1 - 2\kappa_{ip})\boldsymbol{m}_i \otimes \boldsymbol{m}_i + (1 - 2\kappa_{op} - 2\kappa_{ip}\kappa_{op})\boldsymbol{m}_n \otimes \boldsymbol{m}_n \tag{76}$$

where $\boldsymbol{m}_i = \boldsymbol{F}\boldsymbol{M}_i$ and $\boldsymbol{m}_n = \boldsymbol{F}\boldsymbol{M}_n$, respectively. The lower and upper bounds for the in-plane and out-of-plane dispersion parameters are, respectively,

$$0 \leq \kappa_{op} \leq 1/2 \qquad \text{and} \qquad 0 \leq \kappa_{ip} \leq 1 \ . \tag{77}$$

The variation of in-plane and out-of-plane dispersion parameters with respect to the concentration parameters a and b are depicted in Figure 8.

The polar plots of the density distribution and directional stiffness for the HNORS model obtained with the identified parameters for each tissue are depicted in Figure 9. The free-energy functions are identical to the GOH model [34] as depicted in (69). Both GOH model and HNORS models are the extended versions of HGO model and were initially proposed for the arterial wall.

3.3.3 AI-based Alastrué-Martinez-Doblaré-Menzel (AMDM) model

The angular integration-based anisotropic model of Alastrué et al. [1] takes into account rotationally symmetric fiber dispersion based on the micro-sphere model. The model utilizes a planar π-periodic von-Mises distribution for the fiber density distribution $\rho(\boldsymbol{r}, \boldsymbol{M})$ around a mean direction $\boldsymbol{M}$, in the same sense as Gasser et al. [34]. $\boldsymbol{r}$ is the unit orientation vector of a micro-fiber and $\boldsymbol{t} := \boldsymbol{F}\boldsymbol{r}$ is the Eulerian counterpart of the Lagrangian fiber vector. The affine-stretch of a single fiber in the orientation direction $\boldsymbol{r}$ reads

$$\lambda_f := \sqrt{\boldsymbol{t}_\flat \cdot \boldsymbol{t}} \quad \text{where} \quad \boldsymbol{t}_\flat := \boldsymbol{g}\boldsymbol{t} \ . \tag{78}$$

The macroscopic free-energy corresponding to one family of fibers with the mean direction $\boldsymbol{M}$ and with n fibers per unit volume is defined as

$$\Psi_{\mathrm{ani}}(\boldsymbol{g}, \boldsymbol{F}) = \langle \rho\psi_{fib}(\lambda_f)\rangle = \frac{1}{\mid \mathscr{S} \mid}\int_{\mathscr{S}} \rho(\boldsymbol{r};\ \boldsymbol{M})\psi_{fib}(\lambda_f) dA \tag{79}$$

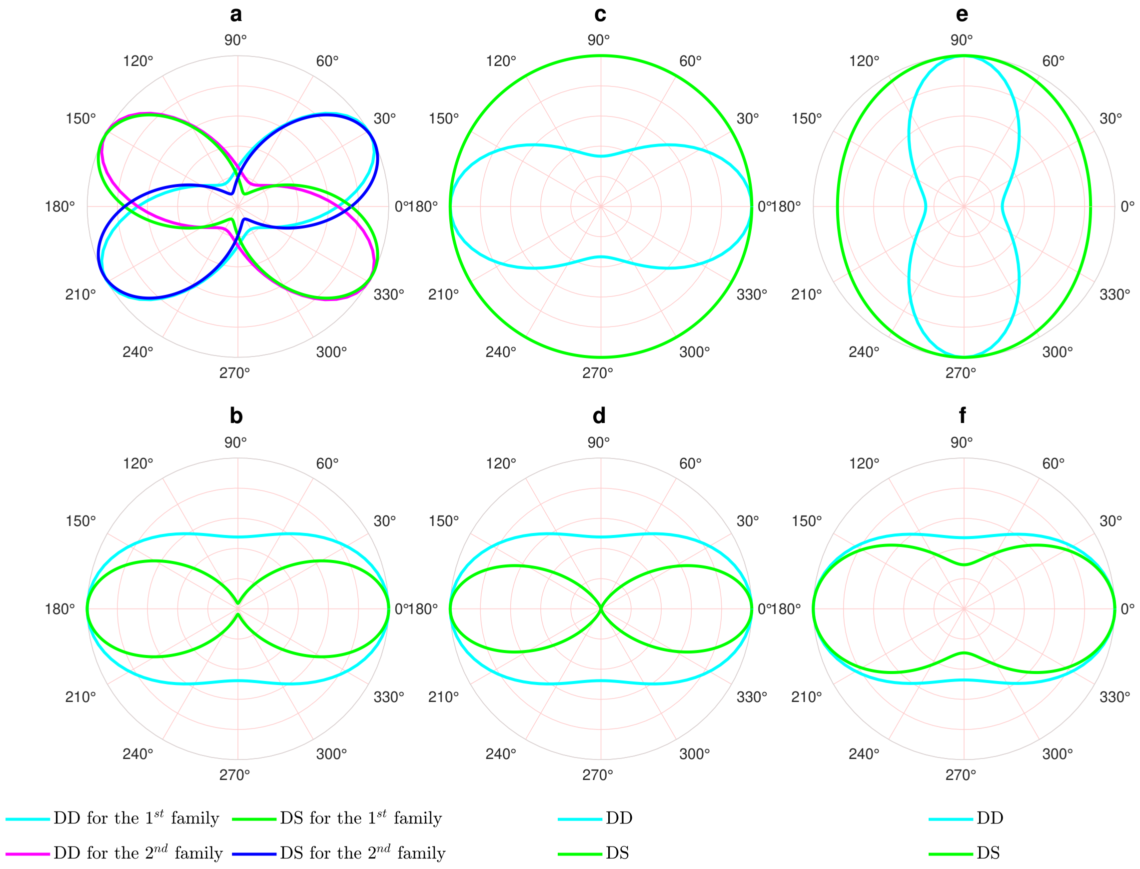

Fig. 9 The polar plots of density distribution (DD) and the directional stiffness (DS) for the HNORS model [46]: (a) in-plane distribution of two families of fibers based on ET dataset for AAA tissue [79], (b) out-of-plane distribution of one families of fibers based on ET dataset for AAA tissue [79] (c) in-plane distribution of one family of fibers based on UT dataset for the linea alba [19], (d) out-of-plane distribution of one family of fibers based on UT dataset for the linea alba [19], (e) in-plane distribution of one family of fibers based on UT dataset for the rectus sheath [70], (f) out-of-plane distribution of one family of fibers based on UT dataset for the rectus sheath [70].

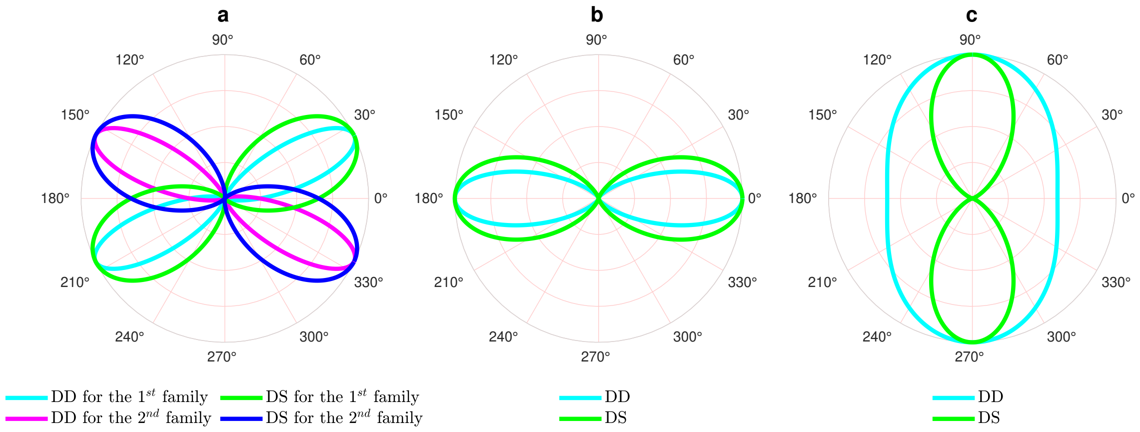

Fig. 10 The polar plots of the density distribution (DD) and the directional stiffness (DS) for the AMDM model [1]: (a) two families of fibers distribution based on ET dataset for AAA tissue [79], (b) one family of fibers distribution based on UT dataset for the linea alba [19], (c) one family of fibers distribution based on UT dataset for the rectus sheath [70].

where ψ_{fib} is the free-energy function associated with the orientation direction $\boldsymbol{r}$ and $|\mathscr{S}| = 4\pi$ for a unit-sphere. For the isotropic ground matrix, they utilized the Neo-Hookean free-energy function. The anisotropic free-energy function is as follows

$$\psi_{fib} = \begin{cases} 0\,, & \text{for } \lambda_f < 1 \\ \dfrac{k_1}{2k_2}[\exp(k_2[\lambda_f^2 - 1]^2) - 1]\,, & \text{for } \lambda_f \geq 1\ . \end{cases} \tag{80}$$

The contribution of each family of fibers to the macroscopic isochoric Kirchhoff stresses can be expressed as a continuous average, including the orientation distribution function, namely

$$\tau_f = \langle \rho \psi_f \bar{\lambda}^{-1} \boldsymbol{t} \otimes \boldsymbol{t} \rangle \quad \text{where} \quad \psi_f := \frac{\partial \psi_{fib}}{\partial \lambda_f} = 2k_1 \lambda_f [\lambda_f^2 - 1] \exp(k_2[\lambda_f^2 - 1]^2)\,. \tag{81}$$

The continuous average in (79) and (81) is approximated by

$$\langle (\bullet) \rangle = \frac{1}{\mid \mathscr{S} \mid} \int_\Omega (\bullet) dA \approx \sum_{i=1}^{m} w^i \, (\bullet)^i \tag{82}$$

where ${w^i}_{i=1,\ldots,m}$ are the weight factors associated with the discrete orientation directions ${\boldsymbol{r}^i}_{i=1,\ldots,m}$. The polar plots of the density distribution and the directional stiffness for the AMDM model obtained with the identified parameters for each tissue are depicted in Figure 10. The rotationally symmetric π-periodic, normalized von-Mises distribution reads

$$\rho(\Theta) = \frac{\bar{\rho}(\Theta)}{I} = 4\sqrt{\frac{b}{4\pi}} \frac{\exp\left(b\cos(2\Theta) + 1\right)}{\mathrm{erfi}\sqrt{2b}}\,. \tag{83}$$

In this regard, the AMDM model can be considered as the AI counterpart of the GOH model.Alastrue et al. [1] originally proposed this model to capture the mechanical response of vascular tissues. They calibrated the material parameters using the human coronary artery data presented by Holzapfel et al. [50].

3.3.4 AI-based Alastrué -Saéz-Martinez-Doblaré (ASMD) model

As an extension of their previous model, Alastrué et al. [2] included the Bingham distribution in their constitutive model. This distribution function exhibits antipodal symmetry and is expressed as

$$\rho(\boldsymbol{r};\ \boldsymbol{Z}, \boldsymbol{Q}) = [F_{0000}(\boldsymbol{Z})]^{-1} \mathrm{etr}(\boldsymbol{Z} \cdot \boldsymbol{Q}^T \boldsymbol{r} \cdot \boldsymbol{r}^T \boldsymbol{Q}) \tag{84}$$

where $\mathrm{etr}(\bullet) \equiv \exp(\mathrm{tr}(\bullet))$, $\boldsymbol{Z}$ is a diagonal matrix with eigenvalues $[\kappa_1, \kappa_2, \kappa_3]$, $\mathbf{Q}$ is orthogonal orientation matrix such that $\boldsymbol{A} = \boldsymbol{Q} \cdot \boldsymbol{Z} \cdot \boldsymbol{Q}^T$ and $F_{0000}(\boldsymbol{Z})$ is defined as

$$F_{0000}(\boldsymbol{Z}) = [4\pi]^{-1} \int_{\mathscr{S}} (\mathrm{etr}(\boldsymbol{Z} : \boldsymbol{r}\boldsymbol{r}^T)\, dA = {}_1F_1(\frac{1}{2};\ \frac{2}{3};\ \boldsymbol{Z}) \tag{85}$$

where ${}_1F_1$ is a confluent hypergeometric function of the matrix argument. The shape of the distribution is controlled by κ_1, κ_2, and κ_3. In this regard, the ASMD model is a slight modification of the AMDM model that utilizes the Bingham distribution, where the density distribution given in (84) replaces π-periodic von-Mises distribution (83) in the equations (79, 81). The polar plots of the density distribution and the directional stiffness for the ASMD model obtained with the identified parameters for each tissue are depicted in Figure 11.

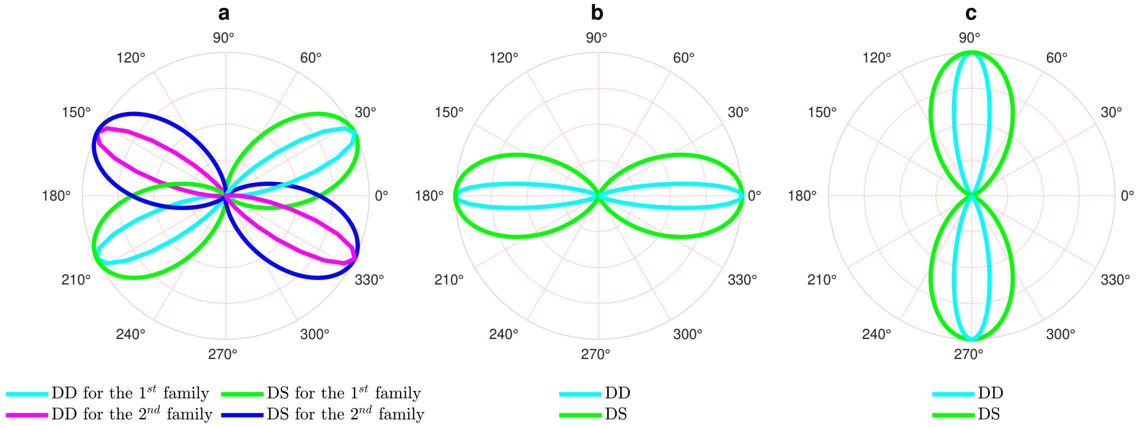

Fig. 11 The polar plots of the density distribution (DD) and the directional stiffness (DS) for the ASMD model [2]: (a) two families of fibers distribution based on ET dataset for AAA tissue [79], (b) one family of fibers distribution based on UT dataset for the linea alba [19], (c) one family of fibers distribution based on UT dataset for the rectus sheath [70].

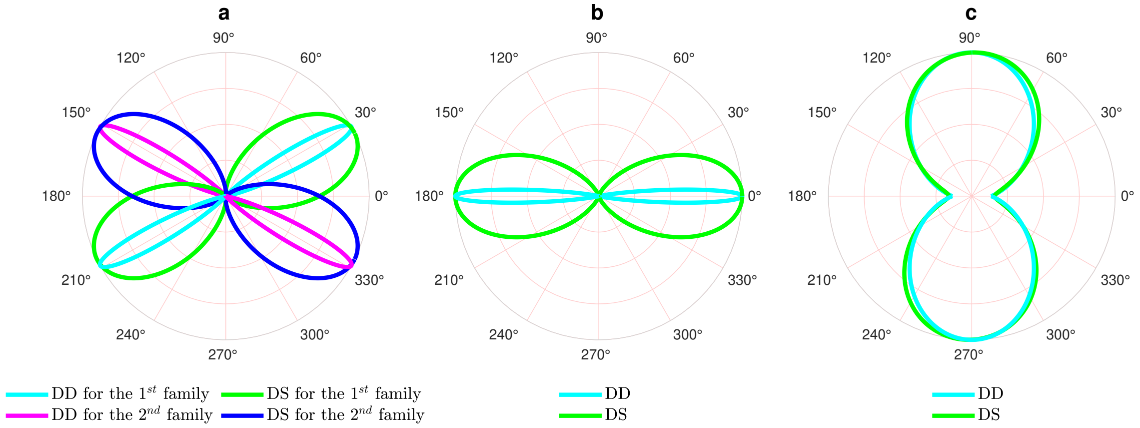

Fig. 12 The polar plots of the density distribution (DD) and the directional stiffness (DS) for the DBB model [24]: (a) two families of fibers distribution based on ET dataset for AAA tissue [79], (b) one family of fibers distribution based on UT dataset for the linea alba [19], (c) one family of fibers distribution based on UT dataset for the rectus sheath [70].

3.3.5 AI-based Driessen-Bouten-Baaijens (DBB) model

Driessen et al. [24] presented an extended version of the Holzapfel et al. [44] (HGO) model which included a fiber volume fraction. They applied the rule of mixtures and expressed the isochoric Kirchhoff stress for multiple fiber directions as follows

$$\boldsymbol{\tau} = \boldsymbol{\tau}^m + \frac{1}{4\pi}\int_{\mathscr{S}} \frac{v_f}{\lambda_f^2}\left(\tau_f - \frac{1}{\lambda_f^2}\boldsymbol{t}\cdot\boldsymbol{\tau}^m\boldsymbol{t}\right)\boldsymbol{t}\otimes\boldsymbol{t}\,dA \tag{86}$$

where $\boldsymbol{\tau}^m$ is the isotropic matrix stress, v_f is the volume fraction of fibers and τ_f is the fiber stress for a given orientation direction $\boldsymbol{r}$. The isotropic matrix material is modeled as a Neo-Hookean material with a shear modulus μ. The stress expressions for the isotropic matrix and fibers are

$$\boldsymbol{\tau}^m = \mu(\boldsymbol{b} - \mathbf{1}) \quad \text{and} \quad \tau_f = k_1\lambda_f^2\left[k_2\exp\left(\lambda_f^2 - 1\right) - 1\right] \; , \tag{87}$$

where the fiber stretch λ_f is given in (78). The DBB model utilizes a planar Gaussian distribution around the mean fiber orientation for the orientation fiber volume

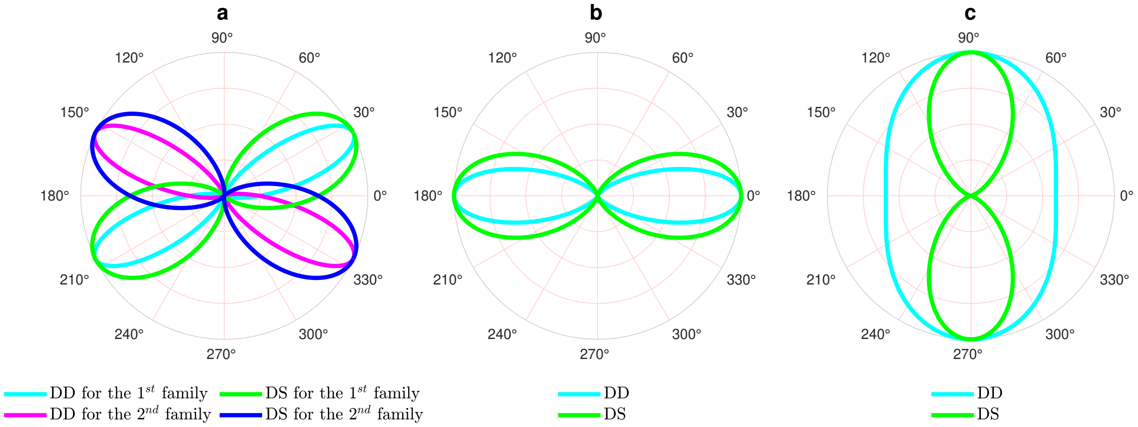

Fig. 13 The polar plots of the density distribution (DD) and the directional stiffness (DS) for LOH model [69]:(a) two families of fiber distribution based on ET dataset for AAA tissue [79], (b) one family of fiber distribution based on UT dataset for linea alba [19], (c) one family of fiber distribution based on UT dataset for rectus sheath [70].

content

$$v_f(\phi) = A\bar{v}_f(\phi) \quad \text{with} \quad \bar{v}_f(\phi) := \exp[\frac{-(\phi-\vartheta)^2}{2\sigma^2}] \tag{88}$$

where ϑ is the mean value, σ is the standard deviation and A is the normalization constant which is defined as

$$\mathrm{A} = \frac{v_{tot}}{\dfrac{1}{\mid \mathscr{S} \mid}\displaystyle\int_{\mathscr{S}} \bar{v}_f(\phi)\, dA}\,. \tag{89}$$

Therein, v_{tot} is the total fiber volume fraction. Unlike the AMDM and ASMD models, the DBB model excludes the volume fraction of the matrix for each orientation direction leading to a structure

$$\frac{1}{\lambda_f^2}\boldsymbol{\tau} : \boldsymbol{t} \otimes \boldsymbol{t} = (1 - v_f)\frac{1}{\lambda_f^2}\boldsymbol{\tau}^m : \boldsymbol{t} \otimes \boldsymbol{t} + v_f \tau_f \tag{90}$$

where, the directional stress additively is decomposed into the matrix contribution and collagen fibers contribution proportional to their volume fraction in each orientation direction, respectively. The polar plots of the density distribution for the DBB model obtained with the identified parameters for each tissue are depicted in Figure 12. Driessen et al. [24] presented this model for aortic valve. As mentioned in the work of Driessen et al [24], the mean fiber direction inside the aortic valve coincide with the principal stretch directions. They calibrated the model using a single family of fiber based on the observations of Billiar and Sacks [10].

3.3.6 AI-based Li-Ogden-Holzapfel (LOH) model

Li et al. [69] proposed an efficient discrete fiber dispersion (DFD) model. Their approach is similar to the model proposed by Alastrue et al. [1], in the sense that both models utilize a von-Mises type planar fiber distribution along with identical free-energy functions for the isotropic and anisotropic parts of the free-energy function. In an attempt to increase the integration accuracy and attain a better resolution of the tension-only condition of the dispersed fibers, Li et al. [69] discretized the unit sphere into a finite number of spherical triangles $\Delta\mathscr{S}_n, n = 1, ..., m$. Accordingly, the fiber directions are associated with the centroids of the spherical triangles. In this work, we have utilized a $m = 640$ point-triangulation as proposed in the original article [69]. The polar plots of the density distribution for the LOH model obtained with the identified parameters for each tissue are depicted in Figure 13.

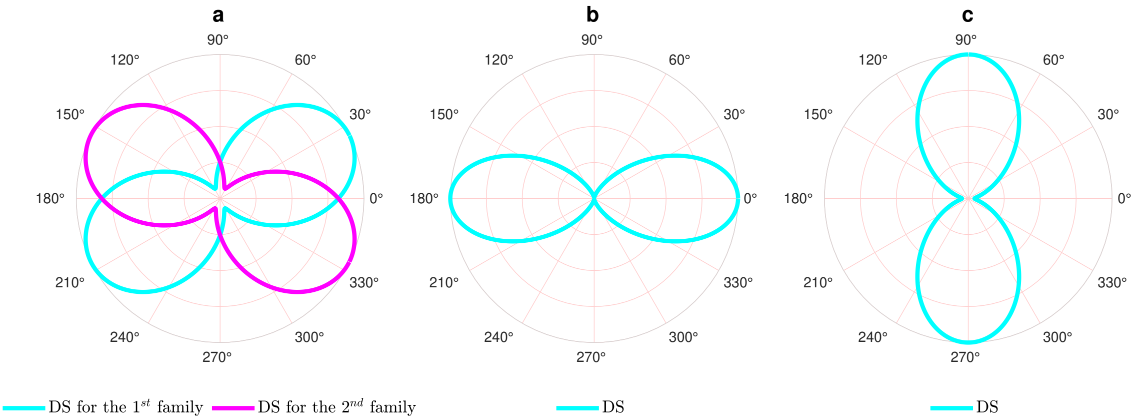

Fig. 14 The directional stiffness (DS) for the ARCCH model [4]: (a) two families of fibers distribution based on ET dataset for AAA tissue [79], (b) one family of fibers distribution based on UT dataset for the linea alba [19], (c) one family of fibers distribution based on UT dataset for the rectus sheath [70].

3.3.7 AI-based Ateshian-Rajan-Chahine-Canal-Hung (ARCCH) model

Ateshian et al. [4] proposed a modeling approach for the matrix of articular cartilage using an angular integration technique with ellipsoidal fiber distribution. The model was considering the osmotic pressure inside the collagen matrix of cartilage besides the fibrous matrix considered with continuous fiber distribution. In this work, we focus on the fiber constitutive relation and fiber angular distribution proposed by Ateshian et al. [4]. They used a power law type free-energy function for fibers as follows

$$\psi_{fib}(\boldsymbol{r};\ \lambda_f^2) = \xi(\boldsymbol{r})(\lambda_f^2 - 1)^{\alpha(\boldsymbol{r})} \quad \text{with} \quad \alpha(\boldsymbol{r}) \geq 2\ , \tag{91}$$

where ξ and α are the material properties that can be evaluated in spherical coordinate system as follows

$$\xi(\boldsymbol{r}) = \left(\frac{\cos^2\theta\ \sin^2\phi}{\xi_1^2} + \frac{\sin^2\theta\ \sin^2\phi}{\xi_2^2} + \frac{\cos^2\theta}{\xi_3^2}\right)\ , \tag{92}$$

$$\alpha(\boldsymbol{r}) = \left(\frac{\cos^2\theta\ \sin^2\phi}{\alpha_1^2} + \frac{\sin^2\theta\ \sin^2\phi}{\alpha_2^2} + \frac{\cos^2\theta}{\alpha_3^2}\right)\ , \tag{93}$$

where ξ_i and $\alpha_i (i = 1, 3)$ are material constants which represents the semi-axes of ellipsoidal. Assuming $\xi_1 = \xi_2 = \xi_3$ and $\alpha_1 = \alpha_2 = \alpha_3$ cover the isotropic case. Ateshian et al. [4] evaluated the continuous integral by discretization of the unit sphere by spherical triangles. In this representation, integral over sphere can be approximated by m number of the spherical triangles as follows

$$\langle(\bullet)\rangle = \frac{1}{\mid \mathscr{S} \mid} \int_{\Omega} (\bullet) dA \approx \sum_{i=1}^{m} (\bullet)^i\, \Delta A_i \tag{94}$$

where ΔA_i is the surface area of the i-th spherical triangle and the quantity $(\bullet)^i$ is evaluated at the centroid of the i-th spherical triangle. The polar plots of the directional stiffness for the ARCCH model obtained with the identified parameters for each tissue are depicted in Figure 14.

4 Parameter Identification and Comparison of Models

4.1 Experimental Studies

In this part, we outline the experiments that are used for the *in silico* investigations made in this paper. To this end, three distinct *human tissues*; (i) the aneurysmatic abdominal aorta, (ii) the linea alba, and (iii) the anterior rectus sheath are selected for the subsequent analysis. The first dataset selected for the investigation is the equibiaxial tension experiment by Niestrawska et al. [79] on human abdominal aortas. They conducted equibiaxial tension experiments on both healthy and aneurysmatic abdominal aortas (AAA). The reason behind the particular choice is twofold. First, it is the single study that performs equibiaxial tension test on human aorta. While the healthy tissue exhibits a more aligned collagen fiber distribution around the mean axis, the media of unhealthy AAA tissue exhibits more dispersed collagen distribution around the mean direction [79]. Eleven wall samples in total were collected from open aneurysm repair at the anterior side. The tests were conducted using a deformation-driven protocol until rupture. This was carried out at a quasi-static strain rate of 3mm/min, and with a stretch ratio of $\lambda_{axial} : \lambda_{circ} = 1 : 1$, where λ_{axial} is the stretch in the axial direction and λ_{circ} is the stretch in the circumferential direction. The experimental data chosen here were from the specimen with the behavior that was approximately median out of all the specimens (specimen AAA-1.2). We pursued our investigation with the median AAA dataset due to the quality of the data (e.g. number of data points in both axis and relatively high rupture stresses allowing ideal S-shaped curve) and the absence of the mechanical stress-strain response for the healthy tissue in the manuscript.

The second and third tissues selected for the investigation are the linea alba and rectus sheath, respectively. Both linea alba and rectus sheath are strong connective tissues made of a single family of collagen fibers dispersed around a mean direction [5, 6]. Linea alba consists of three distinct layers: The ventral linea alba consists of oblique collagen layers. The dorsal part, which is investigated in this study, consists of transversely oriented collagen fibers, exhibiting a distinct anisotropy in its biomechanical properties with the highest compliance in the longitudinal direction and the lowest in the transverse direction [38, 68].[5] Hence, the stiffness variation from the longitudinal direction to the transverse direction is more pronounced in the linea alba. In both tissues, the collagen fibers are densely packed around the mean direction favoring a transverse isotropic response. The uniaxial tensile experiments of Cooney et al. [19], are selected for the investigation of the human linea alba. Seven samples were cut in both the longitudinal and transverse directions. In their investigation, the transverse direction was found to be much stiffer than the longitudinal direction.[6] The third study selected was by Martins et al. [70], who investigated the uniaxial tensile behavior of the human anterior rectus sheath. The histology of the rectus sheath is similar to the linea alba in the sense that the tissues is assumed to

---

[5] Graessel et al. [38] define three layers: ventral, medial, and a thin layer on the dorsal part of linea alba where the collagen distribution is irregular. We follow the description of Levillain et al. [68] omitting the thin layer consisting of irregular collagen fibers on the dorsal surface.

[6] Herein, the term *transverse* refers to the medial-lateral orientation of the abdominal wall, whereas the longitudinal axis refers to the cranio-caudal axis.

exhibit transversely isotropic mechanical response where the longitudinal direction corresponds to the mean orientation of single family of collagen fibers. The tensile behavior was observed to be nonlinear in both the mean fiber and the transverse direction, respectively.

4.2 Parameter identification procedure

The parameter optimization procedure introduced by Dal et al. [20] has been adopted for the constitutive models selected here for anisotropic soft tissues. The parameter identification process is conducted based on error expressions for the uniaxial tension experiments in the $\boldsymbol{e}_1$-direction, uniaxial tension experiments in the $\boldsymbol{e}_2$-direction, and the equibiaxial tension experiment in the $\boldsymbol{e}_1-\boldsymbol{e}_2$ directions,

$$\boldsymbol{\mathcal{E}}_k(\boldsymbol{\zeta}) = \sum_{i=1}^{n_k} \left(P_k(\boldsymbol{\zeta},\lambda_i) - P_k^{exp}(\lambda_i)\right)^2 \ , \quad \text{k=\{UT,ET\}}$$

respectively, where P_k are the first Piola-Kirchhoff stresses, and n_k are number of data points. The total cost function for the UT tests and the ET test are

$$\boldsymbol{\mathcal{E}}_T^{UT}(\boldsymbol{\zeta},\boldsymbol{w}) = w_1\boldsymbol{\mathcal{E}}_{UT_1}(\boldsymbol{\zeta}) + w_2\boldsymbol{\mathcal{E}}_{UT_2}(\boldsymbol{\zeta}), \quad \boldsymbol{\mathcal{E}}_T^{ET}(\boldsymbol{\zeta},\boldsymbol{w}) = w_1\boldsymbol{\mathcal{E}}_{ET_1}(\boldsymbol{\zeta}) + w_2\boldsymbol{\mathcal{E}}_{ET_2}(\boldsymbol{\zeta}). \quad (95)$$

The total cost functions are presented for the UT tests and ET tests individually since there is a lack of UT and ET test data that belong exactly to the same tissue. The parameters are extended to include the weights in (95), $\boldsymbol{\xi} := \{\boldsymbol{\zeta},\boldsymbol{w}\}$ which is obtained from the minimization principle

$$\boldsymbol{\xi} = \text{Arg}\left\{\inf_{\boldsymbol{\xi}\in\mathcal{W}} \mathcal{E}_{\text{TOT}}(\boldsymbol{\xi})\right\} \quad \text{with} \quad \mathcal{W} = \{\boldsymbol{\zeta} \ | \ \boldsymbol{\zeta}\in\mathcal{D} \ \wedge \ \boldsymbol{w} \ | \ w_i \in [0,1]\}\,, \quad (96)$$

where $w_1 + w_2 = 1$. The domain $\mathcal{D}$ is the physically admissible domain for the material parameters $\boldsymbol{\zeta}$.

$$\boldsymbol{\xi} = \textsc{Fmincon}(\mathcal{E}, \boldsymbol{\xi}_0, \boldsymbol{A}, \boldsymbol{b}, \boldsymbol{A}_{\text{eq}}, \boldsymbol{b}_{\text{eq}}) \quad (97)$$

is used to minimize $\mathcal{E}$, subject to the linear equality $\boldsymbol{A}_{\text{eq}}\boldsymbol{\xi} = \boldsymbol{b}_{\text{eq}}$ and inequality $\boldsymbol{A}\boldsymbol{\xi} \leq \boldsymbol{b}$. Therein, $\boldsymbol{A}_{\text{eq}}$ is the coefficient matrix for the equality constraint, $\boldsymbol{b}_{\text{eq}}$ is the vector for the equality constraint, $\boldsymbol{A}$ is the coefficient matrix for the inequality constraints, $\boldsymbol{b}$ is the vector for the inequality constraint, and $\boldsymbol{\xi}_0$ are the initial points.

In this study, a hybrid optimization procedure is employed in order to reach the best parameter set. We utilize the above outlined minimization principle in conjunction with the genetic algorithm presented in Dal et al. [20]. The material parameter space is first trained with the genetic algorithm and the best parameter sets resulting from the genetic algorithm, which correspond to neighbourhood of various local minima, are used as starting points for the gradient search algorithm. This done in order to benefit from the power of genetic algorithm in finding various local minima in nonconvex domain and the power of gradient based algorithms to reduce the cost of genetic algorithms in final iterations.

Discussion: Here, choice of w_1 and w_2 with a constraint $w_1 + w_2 = 1$ is nontrivial. In most experiments, data acquisition in two directions may not be equal, the deformation ranges may not be equal either. Moreover, the tendency of the functional form to fit experiments in two different orientations may not be equal as well. In this respect, even taking $w_1 = w_2 = 0.5$ still may put more emphasis for a certain experiment according to the number of available data. Our experinece, when a certain model does not have the right mathematical form to fit certain direction, treating w_1, w_2 as variables allows the optimization tool to focus on the direction that the model can fit. When comparing the models, the quality of fit does not depend on parameters w_i and the models are sorted according to the same criterion. We initially take $w_i = 0.5$ and observe the optimization toolbox. A model that cannot fit both directions increases the one of the parameters towards 1. We fixed the upper bounds values at various points such as $w_1 = 0.9$ and $w_2 = 0.99$ and checked the quality of fit parameter relative to the case where we fixed $w_1 = 0.5$. We always ended up with better quality of fit for the floating values with upper bounds set to 0.9 and/or 0.99.

4.3 Comparison of hyperelastic anisotropic models

The quality of fit metric χ^2 is used to compare the fitting performance of models. The quality of fit parameter for the uniaxial dataset of Cooney et al. [19], and Martins et al. [70] is

$$\chi^2 = \sum_{i=1}^{n_{UT_1}} \frac{\left(P_{11}^{UT_1}(\lambda_i) - P_{11}^{exp,UT_1}(\lambda_i)\right)^2}{P_{11}^{exp,UT_1}(\lambda_i)} + \sum_{i=1}^{n_{UT_2}} \frac{\left(P_{22}^{UT_2}(\lambda_i) - P_{22}^{exp,UT_2}(\lambda_i)\right)^2}{P_{22}^{exp,UT_2}(\lambda_i)}, \tag{98}$$

where n_{UT_1} and n_{UT_2} are the number of data points and $P_{11}^{UT_1}$ and $P_{22}^{UT_2}$ are the first Piola-Kirchhoff stresses for the UT test in the $\boldsymbol{e}_1$ and $\boldsymbol{e}_2$ directions, respectively. Similarly, for the equibiaxial loading case, the quality of fit parameter for the fitting of the Niestrawska et al. [79] dataset is

$$\chi^2 = \sum_{i=1}^{n_{ET}} \frac{\left(P_{11}^{ET}(\lambda_i) - P_{11}^{exp,ET}(\lambda_i)\right)^2}{P_{11}^{exp,ET_1}(\lambda_i)} + \sum_{i=1}^{n_{ET}} \frac{\left(P_{22}^{ET}(\lambda_i) - P_{22}^{exp,ET}(\lambda_i)\right)^2}{P_{22}^{exp,ET_2}(\lambda_i)}, \tag{99}$$

where n_{ET} is the number of data points and $P_{11}^{ET_1}$ and P_{22}^{ET} are the first Piola-Kirchhoff stresses for the ET test in the $\boldsymbol{e}_1 - \boldsymbol{e}_2$ directions. The quality of fit metric for each model has been presented in three regions based on the stretch ranges,

$$\mathrm{reg}_1 := \lambda \in [1, 1/3\lambda_{\max}], \quad \mathrm{reg}_2 := \lambda \in [1, 2/3\lambda_{\max}], \quad \mathrm{reg}_3 := \lambda \in [1, \lambda_{\max}]. \tag{100}$$

Comparison of the models based on alternative statistics metrics such as the root mean square error (RMSE) and the coefficient of determination (R^2) can be found in the Appendix.

5 Results and discussion

The models are compared based on their quality of fit metric using the ET dataset for AAA tissue [79], UT dataset for the linea alba [19], and UT dataset for the rectus sheath [70]. Figures 15–17 depict the simultaneous fit results of the each model to three datasets. In the parameter optimization procedure, we have adhered to the histological information provided by Niestrawska et al. [79], Cooney et al. [19], and Martins et al. [70] in that, for each model, we have imposed the same mean fiber directions. However, due to the lack of histological data on the fiber dispersion, we

Table 2 Models sorted according to the *quality of fit* to the equibiaxial dataset of AAA tissue [79], uniaxial dataset of the linea alba [19] and uniaxial dataset of the rectus sheath [70].

	AAA tissue				**linea alba**				**rectus sheath**			
rank	**model name**	**model type**	χ^2	*nop*	**model name**	**model type**	χ^2	*nop*	**model name**	**model type**	χ^2	*nop*
1	HNORS model [46]	GST	2.4368	6	ARCCH model [4]	AI	0.4136	6	ARCCH model [4]	AI	0.0642	6
2	HSGR model [50]	I_1, I_4	2.4734	5	HNORS model [46]	GST	0.7075	5	NY model [71]	I_1, I_4	0.0949	4
3	LOH model [69]	AI	2.4945	5	HY model [56]	I_1, I_4	0.8739	4	ASMD model [2]	AI	0.6011	5
4	AMDM model [1]	AI	2.8541	5	ASMD model [2]	AI	0.9159	5	AMDM model [1]	AI	0.7563	5
5	GOH model [34]	GST	3.3643	5	AMDM model [1]	AI	0.9163	5	LOH model [69]	AI	1.0750	5
6	ASMD model [2]	AI	3.7984	6	LOH model [69]	AI	0.9427	5	HY model [56]	I_1, I_4	1.1202	4
7	DBB model [24]	AI	10.0814	6	DBB model [24]	AI	1.0002	6	DBB model [24]	AI	1.8341	6
8	HY model [56]	I_1, I_4	10.1666	4	HSGR model [50]	I_1, I_4	1.0468	5	HSGR model [50]	I_1, I_4	3.3545	5
9	NY model [71]	I_1, I_4	11.0814	4	OS model [80]	I_1, I_4	1.1294	6	OS model [80]	I_1, I_4	3.3823	6
10	ARCCH model [4]	AI	25.179	6	GOH model [34]	GST	1.2228	4	HNORS model [46]	GST	3.6038	6
11	HGO model [44]	I_1, I_4	47.4992	4	HGO model [44]	I_1, I_4	1.2529	4	GOH model [34]	GST	3.6722	4
12	OS model [80]	I_1, I_4	86.1323	5	NY model [71]	I_1, I_4	11.3349	4	HGO model [44]	I_1, I_4	3.7582	4

decided to treat the distribution parameters as model parameters to be determined during the parameter identification procedure. Ideally, the fiber density distributions shall be obtained from histological information gathered from various visualization techniques such as second harmonic generation [16, 84], X-ray diffraction [72], or polarized light microscopy [85]. For twelve anisotropic models, identified parameters and error bounds for AAA tissue, linea alba, and rectus sheath can be found in Appendix.

AAA tissue: Using the ET dataset for AAA tissue [79], the models are sorted regarding the quality of fit metric, and the results are listed in Table 2(column #1). The ET dataset for AAA tissue was obtained from an arterial wall specimen with two families of fibers. All models except the HGO [44], OS [80] and ARCCH [4] models fit the AAA tissue quite successfully, see Figure 15. The OS model overpredicts the linear phase of the stress-stretch relation and fails to capture the transition from a linear phase to an exponential phase for the curves in both the axial and circumferential directions. On the other hand, the HGO model fail to simultaneously predict the equibiaxial stress-stretch behavior in both the circumferential and axial directions whereas they are capable of fitting either the circumferential or axial stress-stretch behavior successfully. The ARCCH model demonstrates that the single power term in the free-energy is not as successful as the Fung-type functional representations. The first six models, which were particularly designed to predict arterial wall response, showed a remarkable fitting performance to the ET dataset of AAA tissue [1, 2, 24, 34, 46, 50, 71]. It can be easily seen that the models having a Fung-type exponential free-energy and models taking the fiber dispersion into account are relatively more successful. The only invariant based model that has considerably superior modeling performance relative to the other invariant forms is the HSGR model. This model uses a mixed invariant term in the anisotropic part in terms of I_1 and I_4 where the parameter p controls the contribution of each part. Hence, this allows and additional Fung-type contribution to the isotropic matrix response which is not the case in other invariant-based formulations. In this regard, HSGR model can be considered as a psuedo-GST model. The most successful model according to the fitting performance of the AAA tissue ET dataset is the six-parameter HNORS model [46] based on the bivariate von-Mises distribution that considers the in- and out-of-plane dispersion of fibers. The five-parameter HSGR model, and the four-parameter NY model [71] also exhibit a remarkable fitting performance with fewer

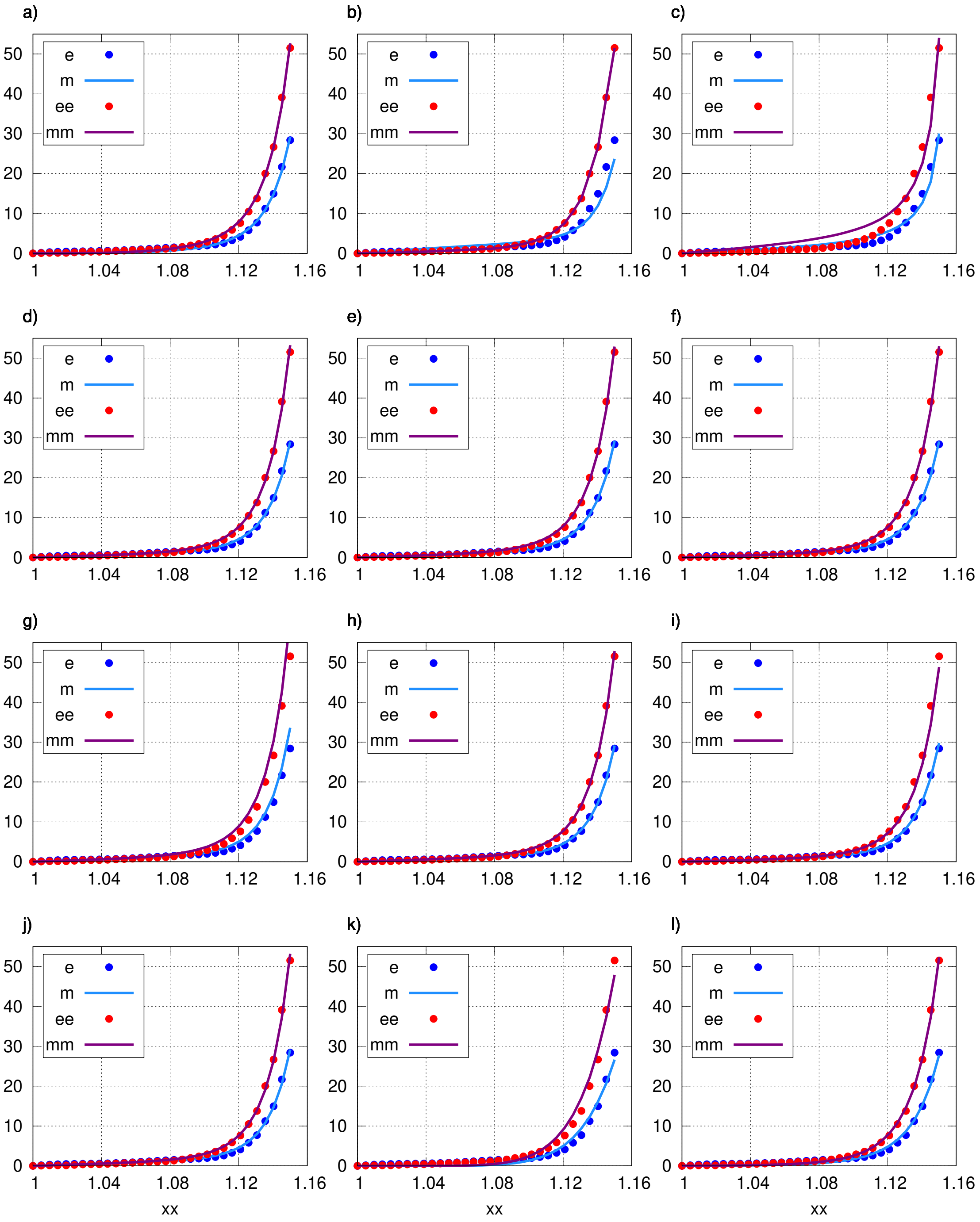

Fig. 15 a) NY model [71], b) HGO model [44], c) OS model [80], d) HSGR model [50], e) GOH model [34], f) HNORS model [46], g) DBB model [24], h) AMDM model [1], i) ASMD model [2], j) LOH model [69], k) ARCCH model [4], l) HY model [56] predictions for ET dataset for AAA tissue [79].

material parameters. AI-based LOH [69], AMDM [1] and GST-based GOH models [34] also demonstrated excellent fitting performance; these models consider fiber dispersion with an identical von-Mises distribution function and use an equivalent free-energy function. The only difference between these models is the integration approach. Their fitting performance is almost equivalent, however, the computational cost of the GOH model is significantly less compared to the AMDM and LOH model, see also [48]. The discrete integration algorithm proposed in LOH models

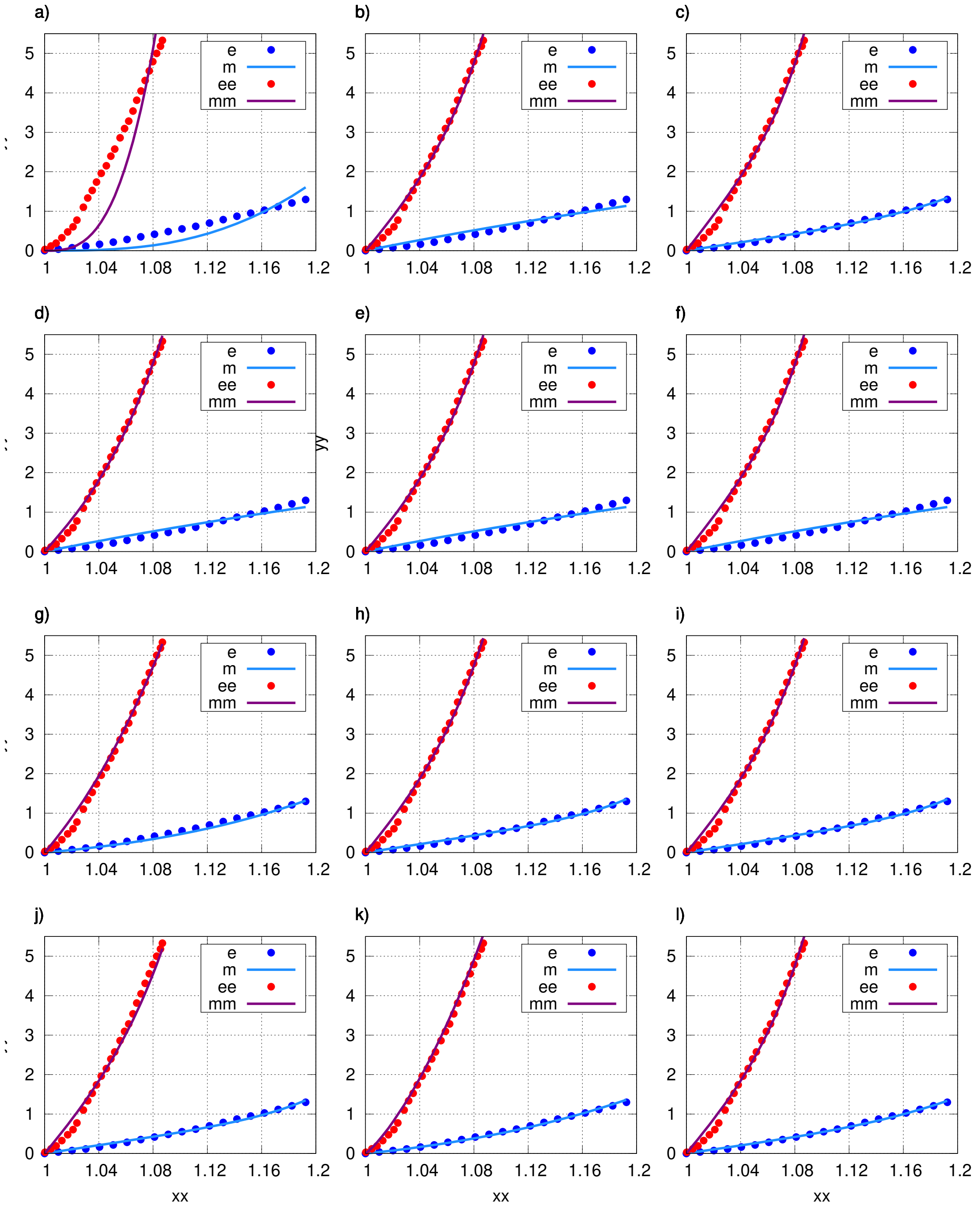

Fig. 16 a) NY model [71], b) HGO model [44], c) OS model [80], d) HSGR model [50], e) GOH model [34], f) HNORS model [46], g) DBB model [24], h) AMDM model [1], i) ASMD model [2], j) LOH model [69], k) ARCCH model [4], l) HY model [56] predictions for UT dataset for linea alba [19].

slightly improves its behaviour over AMDM model, however, the additional computational cost is also high.

Linea alba: The fitting performance of the models based on the UT dataset for the linea alba is listed in Table 2(column #2). The stress stretch curves for linea alba exhibits a power/exponential form in both mutually orthogonal axes. The model predictions for the stress-stretch curves of all models are depicted in Figure 16.

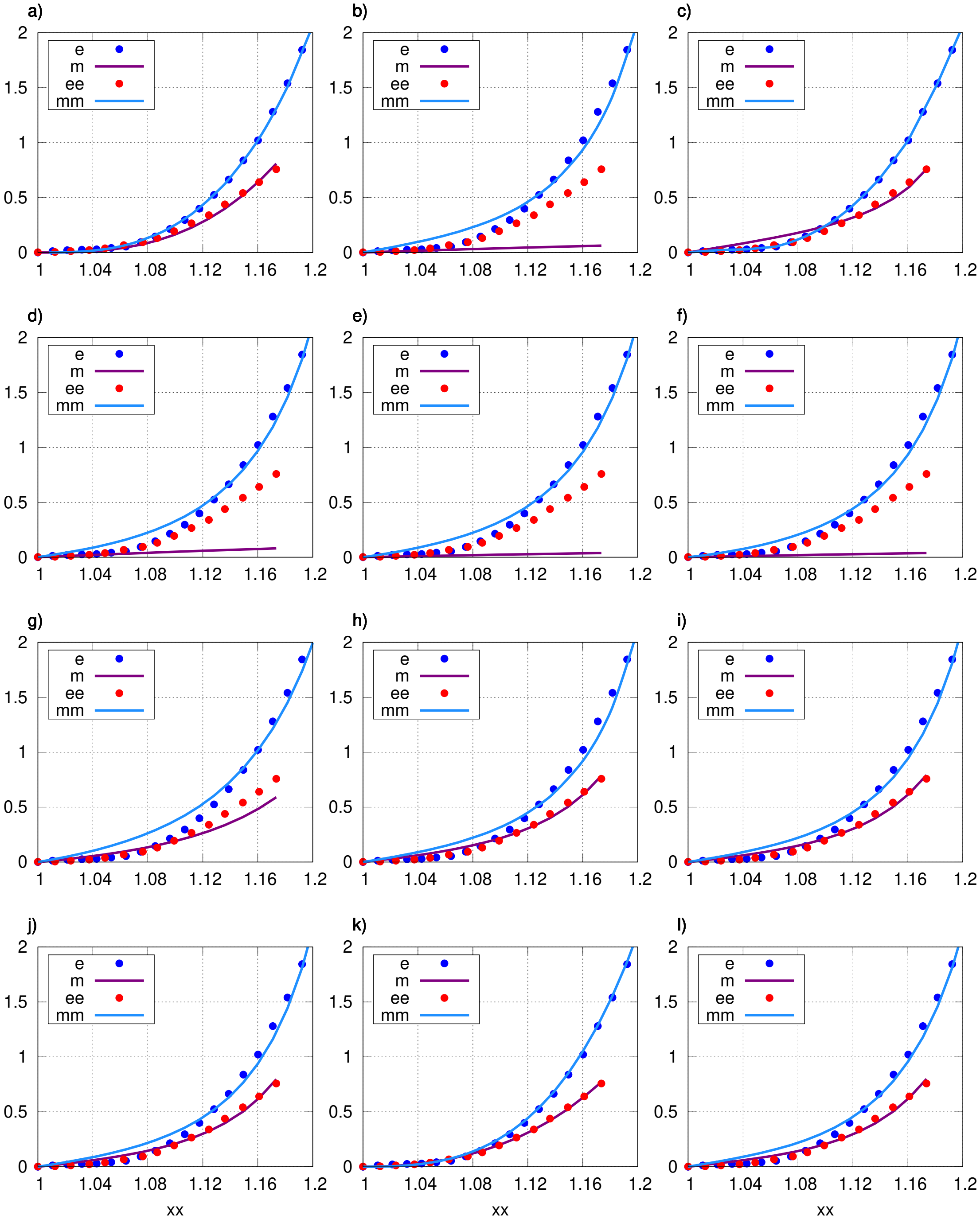

Fig. 17 a) NY model [71], b) HGO model [44], c) OS model [80], d) HSGR model [50], e) GOH model [34], f) HNORS model [46], g) DBB model [24], h) AMDM model [1], i) ASMD model [2], j) LOH model [69], k) ARCCH model [4], l) HY model [56] predictions for UT dataset for rectus sheath [70].

The ARCCH model [4] with power-type free-energy function exhibits the best performance among all. The model was originally proposed for articular cartilage, a connective tissue, as linea alba. Among all invariant-based formulations, HY model [56] with isotropic matrix and exponential anisotropic fibre response exhibits the best fitting performance. The fibre bundles of human linea alba are densely oriented in transverse direction and exhibit less than 10 % reorientation during tensile test and the mechanical response, governed by elastin in longitudinal direction, remains nearly linear [68]. Hence, the transversely isotropic structure and the specific form of the free-energy function of HY model provides an excellent mathematical format for linea alba.

Rectus sheath: The rectus sheath tissue exhibits a relatively softer mechanical response with a weaker degree of anisotropy. The models are sorted according to the quality of fit metric and are listed in Table 2(column #3). It can be observed that, unlike linea alba, the stretch-stress response of the rectus sheath tissue is nonlinear in both transverse and longitudinal directions. The model predictions for stress-stretch curves of all models are depicted in Figure 17. The ARCCH model [4] exhibits the best fitting performance followed by The NY model [71] with an almost excellent fitting performance. When considering all tweleve models, the ARCCH and NY models are the only models which do not decompose the free-energy function into distinct isotropic part and anisotropic parts. Recall that both NY and ARCCH models were originally proposed for mitral valve and articular cartilage, both abundant in connective tissues. Transversely isotropic models such as the HGO model cannot capture this mechanical response, since the non-fibrous part of the tissue is modeled by the Neo-Hookean model. However, another transversely isotropic model, the OS model [80] is able to show better fitting performance than the HGO model as the isotropic base matrix is modeled by a nonlinear free-energy function. Furthermore, GST-based dispersion models have weak performance on rectus sheath data. GST-based dispersion models such as GOH [34] and HNORS [46] models impose tension only condition for mean fiber directions. However, in the case of rectus sheath, the mean direction of fibers is along longitudinal direction and as a result GOH [34] and HNORS [46] models are reduced to Neo-Hookean model to predict mechanics behavior along transverse direction to the fibers. The same behavior can also be seen in HGO [44], HSGR [50] models.

Summary: The comparison of the results demonstrate that the fiber dispersion-based models have a superior fitting performance over the strain invariant-based models for arterial wall where the fiber dispersion is observed both for aneursymatic and healthy tissues. GST-based dispersion models are more cost efficient compared to the AI-based dispersion formulations regarding the computational time. On the other hand, the quality of fit of AI- and GST-based formulations are comparable for AAA tissue, see for example the AMDM [1] and GOH [34] models. This is inline with the results of Holzapfel & Ogden [48] obtained from uniaxial tension experiments of (adventitia) healthy abdominal aorta. It is to be noted that, qualitatively equivalent macroscopic stress-stretch response of these two models is with different dispersion parameters. LOH model, which proposes a discrete fiber orientation approach that improves the numerical integration on spherical domain along with improved algorithm for imposition of tension-only condition, improves fitting quality of AMDM approach slighlty for AAA tissue. AMDM and LOH models provide nearly identical predictions for linea alba and rectus sheath as the fibers are more aligned. GST-based approaches require special attention regarding the imposition of the tension-only condition [47, 67]. Moreover, AI-based formulations are able to adapt themselves for a variety of tissues having different families of fiber architecture. The OS model [80], based on the functional form of the Gent model originally proposed for the non-Gaussian chain statistics of the rubber network, is not as successful as the models based on the Fung-type exponential representations for the anisotropic part of the free-energy function, see for example HSGR [50], GOH [34], and AMDM [1] models. Fung-type exponential form of free-energy function is superior to other forms in modeling stress-stretch response of arterial wall. On the other hand, the power-form of free-energy function in the form of ARCCH model [4] provides excellent form for the stress-stretch response of connective tissues. For the effective use of dispersion-type anisotropic formulations, more scientific data that provides standardized visualization techniques [16] along with mechanical test is important.

Conflict of interest: The authors declare that they have no conflict of interest.

References

[1] Alastrué, V., M. Martinez, M. Doblaré, and A. Menzel. 2009. Anisotropic microsphere-based finite elasticity applied to blood vessel modelling. *Journal of the Mechanics and Physics of Solids 57*(1): 178–203 .

[2] Alastrué, V., P. Sáez, M. Martínez, and M. Doblaré. 2010. On the use of the bingham statistical distribution in microsphere-based constitutive models for arterial tissue. *Mechanics Research Communications 37*(8): 700–706 .

[3] Ateshian, G.A. 2007. Anisotropy of Fibrous Tissues in Relation to the Distribution of Tensed and Buckled Fibers. *Journal of Biomechanical Engineering* 129: 240–249 .

[4] Ateshian, G.A., V. Rajan, N.O. Chahine, C.E. Canal, and C.T. Hung. 2009. Modeling the matrix of articular cartilage using a continuous fiber angular distribution predicts many observed phenomena. *Journal of Biomechanical Engineering 131*(6): 061003 .

[5] Axer, H., D.G. v. Keyserlingk, and A. Prescher. 2001a. Collagen fibers in linea alba and rectus sheaths: I. general scheme and morphological aspects. *Journal of Surgical Research 96*(1): 127–134 .

[6] Axer, H., D.G. v. Keyserlingk, and A. Prescher. 2001b. Collagen fibers in linea alba and rectus sheaths: Ii. variability and biomechanical aspects. *Journal of Surgical Research 96*(2): 239–245 .

[7] Balzani, D., P. Neff, J. Schröder, and G.A. Holzapfel. 2006. A polyconvex framework for soft biological tissues. adjustment to experimental data. *International journal of solids and structures 43*(20): 6052–6070 .

[8] Beatty, M.F. 1987. Topics in finite elasticity: Hyperelasticity of rubber, elastomers, and biological tissues—with examples. *Applied Mechanics Reviews 40*(12): 1699 .

[9] Bhattarai, A., W. Kowalczyk, and T.N. Tran. 2021. A literature review on large intestinal hyperelastic constitutive modeling. *Clinical Biomechanics* 88: 105445 .

[10] Billiar, K.L. and M.S. Sacks. 2000. Biaxial mechanical properties of the natural and glutaraldehyde treated aortic valve cusp—part i: experimental results. *Journal of biomechanical engineering 122*(1): 23–30 .

[11] Budday, S., G. Sommer, C. Birkl, C. Langkammer, J. Haybaeck, J. Kohnert, M. Bauer, F. Paulsen, P. Steinmann, E. Kuhl, et al. 2017. Mechanical characterization of human brain tissue. *Acta Biomaterialia* 48: 319–340 .

[12] Cansız, B., H. Dal, and M. Kaliske. 2017. Computational cardiology: A modified hill model to describe the electro-visco-elasticity of the myocardium. *Computer Methods in Applied Mechanics and Engineering* 315: 434–466 .

[13] Cansız, B., H. Dal, and M. Kaliske. 2018. Computational cardiology: the bidomain based modified hill model incorporating viscous effects for cardiac defibrillation. *Computational Mechanics* 62: 253–271 .

[14] Cansız, F.B.C., H. Dal, and M. Kaliske. 2015. An orthotropic viscoelastic material model for passive myocardium: theory and algorithmic treatment. *Computer Methods in Biomechanics and Biomedical Engineering* 18: 1160–1172 .

[15] Chagnon, G., M. Rebouah, and D. Favier. 2015. Hyperelastic energy densities for soft biological tissues: a review. *Journal of Elasticity 120*(2): 129–160 .

[16] Chen, X., O. Nadiarynkh, S. Plotnikov, and P.J. Campagnola. 2012. Second harmonic generation microscopy for quantitative analysis of collagen fibrillar structure. *Nature Protocols 7*(4): 654–669 .

[17] Choi, H.S. and R. Vito. 1990. Two-dimensional stress-strain relationship for canine pericardium. *Journal of biomechanical engineering 112*(2): 153–159 .

[18] Chuong, C. and Y. Fung. 1983. Three-dimensional stress distribution in arteries. *Journal of biomechanical engineering 105*(3): 268–274 .

[19] Cooney, G.M., S.P. Lake, D.M. Thompson, R.M. Castile, D.C. Winter, and C.K. Simms. 2016. Uniaxial and biaxial tensile stress-stretch response of human linea alba. *Journal of the mechanical behavior of biomedical materials* 63: 134–140 .

[20] Dal, H., K. Açıkgöz, and Y. Badienia. 2021. On the performance of isotropic hyperelastic constitutive models for rubber-like materials: a state of the art review. *Applied Mechanics Reviews 73*(2): 020802 .

[21] Dal, H., S. Göktepe, E. Kuhl, and M. Kaliske. 2013. A fully implicit finite element method for bidomain models of cardiac electromechanics. *Computer Methods in Applied Mechanics and Engineering* 253: 323–336 .

[22] Dal, H., O. Gültekin, and K. Açıkgöz. 2020. An extended eight-chain model for hyperelastic and finite viscoelastic response of rubberlike materials: Theory, experiments and numerical aspects. *Journal of the Mechanics and Physics of Solids* 145: 104159 .

[23] Demiray, H. and R. Vito. 1976. Large deformation analysis of soft biomaterials. *International Journal of Engineering Science 14*(9): 789–793 .

[24] Driessen, N.J., C.V. Bouten, and F.P. Baaijens. 2005. A structural constitutive model for collagenous cardiovascular tissues incorporating the angular fiber distribution. *Journal of Biomechanical Engineering 127*(3): 494–503 .

[25] Durcan, C., M. Hossain, G. Chagnon, D. Peric, L. Bsiesy, G. Karam, and E. Girard. 2022a. Experimental investigations of the human oesophagus: anisotropic properties of the embalmed mucosa-submucosa layer under large deformation. *Biomechanics and Modeling in Mechanobiology* 21: 1169–1186 .

[26] Durcan, C., M. Hossain, G. Chagnon, D. Peric, L. Bsiesy, G. Karam, and E. Girard. 2022b. Experimental investigations of the human oesophagus: anisotropic properties of the embalmed muscular layer under large deformation. *Biomechanics and Modeling in Mechanobiology* 21: 1169–1186 .

[27] Durcan, C., M. Hossain, G. Chagnon, D. Peric, and E. Girard. 2023. Characterisation of the layer, direction and time-dependent mechanical behaviour of the human oesophagus and the effects of formalin preservation. *Acta Biomaterialla*: In Press .

[28] Egorov, V.I., I.V. Schastlivtsev, E.V. Prut, A.O. Baranov, and R.A. Turusov. 2002. Mechanical properties of the human gastrointestinal tract. *Journal of Biomechanics 35*(10): 1417–1425 .

[29] Ferrara, A., S. Morganti, P. Totaro, A. Mazzola, and F. Auricchio. 2016. Human dilated ascending aorta: mechanical characterization via uniaxial tensile tests. *Journal of the Mechanical Behavior of Biomedical Materials* 53: 257–271 .

[30] Fung, Y. 1967. Elasticity of soft tissues in simple elongation. *American Journal of Physiology-Legacy Content 213*(6): 1532–1544 .

[31] Fung, Y., K. Fronek, and P. Patitucci. 1979. Pseudoelasticity of arteries and the choice of its mathematical expression. *American Journal of Physiology-Heart and Circulatory Physiology 237*(5): H620–H631 .

[32] Fung, Y.C. 1993. *Biomechanics: Mechanical Properties of Living Tissues.* Springer, New York.

[33] Fung, Y.C. 1994. *A First Course in Continuum Mechanics for Physical and Biological Engineers and Scientists.* Prentice Hall, Englewood Cliffs, New Jersey.

[34] Gasser, T.C., R.W. Ogden, and G.A. Holzapfel. 2006. Hyperelastic modelling of arterial layers with distributed collagen fibre orientations. *Journal of the royal society interface 3*(6): 15–35 .

[35] Gent, A.N. 1996. A new constitutive relation for rubber. *Rubber chemistry and technology 69*(1): 59–61 .

[36] Ghaemi, H., K. Behdinan, and A. Spence. 2009. In vitro technique in estimation of passive mechanical properties of bovine heart: Part i. experimental techniques and data. *Medical engineering & physics 31*(1): 76–82 .

[37] Girard, E., G. Chagnon, E. Gremen, M. Calvez, C. Masri, J. Boutonnat, B. Trilling, and B. Nottelet. 2019. Biomechanical behaviour of human bile duct wall and impact of cadaveric preservation processes. *Journal of the Mechanical Behavior of Biomedical Materials* 98: 291–300 .

[38] Graessel, D., A. Prescher, S. Fitzek, D.G. v. Keyserlingk, and H. Axer. 2005. Anisotropy of human linea alba: A biomechanical study. *Journal of Surgical Research 124*(1): 118–125 .

[39] Groves, R.B., S.A. Coulman, J.C. Birchall, and S.L. Evans. 2013. An anisotropic, hyperelastic model for skin: experimental measurements, finite element modelling and identification of parameters for human and murine skin. *Journal of the Mechanical Behavior of Biomedical Materials* 18: 167–180 .

[40] Gültekin, O., H. Dal, and G.A. Holzapfel. 2019. On the quasi-incompressible finite element analysis of anisotropic hyperelastic materials. *Computational mechanics 63*(3): 443–453 .

[41] Gültekin, O., B. Rodoplu, and H. Dal. 2020. A quasi-incompressible and quasi-inextensible finite element analysis of fibrous soft biological tissues. *Biomechanics and Modeling in Mechanobiology 19*(6): 2357–2373 .

[42] Hayashi, K. 1993. Experimental Approaches on Measuring the Mechanical Properties and Constitutive Laws of Arterial Walls. *Journal of Biomechanical Engineering 115*(4B): 481–488 .

[43] Holzapfel, G.A. 2000. *Nonlinear Solid Mechanics: A Continuum Approach for Engineering*. Johnn Wiley & Sons, Chichester.

[44] Holzapfel, G.A., T.C. Gasser, and R.W. Ogden. 2000. A new constitutive framework for arterial wall mechanics and a comparative study of material models. *Journal of elasticity and the physical science of solids 61*(1): 1–48 .

[45] Holzapfel, G.A., T.C. Gasser, and R.W. Ogden. 2004. Comparison of a Multi-Layer Structural Model for Arterial Walls With a Fung-Type Model, and Issues of Material Stability. *Journal of Biomechanical Engineering 126*(2): 264–275 .

[46] Holzapfel, G.A., J.A. Niestrawska, R.W. Ogden, A.J. Reinisch, and A.J. Schriefl. 2015. Modelling non-symmetric collagen fibre dispersion in arterial walls. *Journal of the royal society interface 12*(106): 20150188 .

[47] Holzapfel, G.A. and R.W. Ogden. 2015. On the tension–compression switch in soft fibrous solids. *European Journal of Mechanics - A/Solids* 49: 561–569 .

[48] Holzapfel, G.A. and R.W. Ogden. 2017. Comparison of two model frameworks for fiber dispersion in the elasticity of soft biological tissues. *European Journal of*

Mechanics-A/Solids 66: 193–200 .

[49] Holzapfel, G.A., R.W. Ogden, and S. Sherifova. 2019. On fibre dispersion modelling of soft biological tissues: a review. *Proceedings of the Royal Society A 475*(2224): 20180736 .

[50] Holzapfel, G.A., G. Sommer, C.T. Gasser, and P. Regitnig. 2005. Determination of layer-specific mechanical properties of human coronary arteries with nonatherosclerotic intimal thickening and related constitutive modeling. *American Journal of Physiology-Heart and Circulatory Physiology 289*(5): H2048–H2058 .

[51] Holzapfel, G.A. and H.W. Weizsäcker. 1998. Biomechanical behavior of the arterial wall and its numerical characterization. *Computers in biology and medicine 28*(4): 377–392 .

[52] Horgan, C.O. and G. Saccomandi. 2005. A new constitutive theory for fiber-reinforced incompressible nonlinearly elastic solids. *Journal of the Mechanics and Physics of Solids 53*(9): 1985–2015 .

[53] Hossain, M., A.F.M.S. Amin, and N. Kabir. 2015. Eight-chain and full-network models and their modified versions for rubber hyperelasticity: a comparative study. *Journal of the Mechanical Behavior of Materials 24*(1-2): 11–24 .

[54] Hossain, M. and P. Steinmann. 2013. More hyperelastic models for rubber-like materials: consistent tangent operators and comparative study. *Journal of the Mechanical Behavior of Materials 22*(1-2): 27–50 .

[55] Hossain, M., D.K. Vu, and P. Steinmann. 2012. Experimental study and numerical modelling of vhb 4910 polymer. *Computational Materials Science* 59: 65–74 .

[56] Humphrey, J. and F. Yin. 1987. On constitutive relations and finite deformations of passive cardiac tissue: I. a pseudostrain-energy function. *Journal of biomechanical engineering 109*(4): 298–304 .

[57] Humphrey, J.D. 1995. Mechanics of the arterial wall: review and directions. *Critical Reviews in Biomedical Engineering 23*(1-2): 1–162 .

[58] Humphrey, J.D. 2002. *Cardiovascular Solid Mechanics: Cells, Tissues, and Organs.* Springer, New York.

[59] Humphrey, J.D., R.K. Strumpf, and F.C.P. Yin. 1990. Determination of a constitutive relation for passive myocardium: I. a new functional form. *Journal of Biomechanical Engineering 112*(3): 333–339 .

[60] Kadapa, C. and M. Hossain. 2022. A linearised consistent mixed displacement-pressure formulation for hyperelasticity. *Mechanics of Advanced Materials and Structures 29*(2): 267–284 .

[61] Kalra, A., A. Lowe, and A. Al-Jumaily. 2016. Mechanical behaviour of skin: a review. *Journal of Material Sciences and Engineering 5*(4): 1000254 .

[62] Kas' yanov, V. and A. Rachev. 1980. Deformation of blood vessels upon stretching, internal pressure, and torsion. *Mechanics of Composite Materials 16*(1): 76–80 .

[63] Kemper, A.R., A.C. Santago, J.D. Stitzel, J.L. Sparks, and S.M. Duma. 2012. Biomechanical response of human spleen in tensile loading. *Journal of Biomechanics 45*(2): 348–355 .

[64] Lanir, Y. 1979. A structural theory for the homogeneous biaxial stress-strain relationships in flat collagenous tissues. *Journal of Biomechanics 12*(6): 423–436 .

[65] Lanir, Y. 1983. Constitutive equations for fibrous connective tissues. *Journal of Biomechanics 16*(1): 1–12 .

[66] Lanir, Y. 1987. Biorheology and Fluid Flux in Swelling Tissues. II. Analysis of Unconfined Compressive Response of Transversely Isotropic Cartilage Disc. *Biorheology 24*(2): 189–205 .

[67] Latorre, M. and F.J. Montáns. 2016. On the tension-compression switch of the gasser–ogden–holzapfel model: Analysis and a new pre-integrated proposal. *Journal of the Mechanical Behavior of Biomedical Materials* 57: 175–189 .

[68] Levillain, A., M. Orhant, F. Turquier, and T. Hoc. 2016. Contribution of collagen and elastin fibers to the mechanical behavior of an abdominal connective tissue. *Journal of the Mechanical Behavior of Biomedical Materials* 61: 308–317 .

[69] Li, K., R.W. Ogden, and G.A. Holzapfel. 2018. A discrete fibre dispersion method for excluding fibres under compression in the modelling of fibrous tissues. *Journal of The Royal Society Interface 15*(138): 20170766 .

[70] Martins, P., E. Peña, R.N. Jorge, A. Santos, L. Santos, T. Mascarenhas, and B. Calvo. 2012. Mechanical characterization and constitutive modelling of the damage process in rectus sheath. *Journal of the mechanical behavior of biomedical materials* 8: 111–122 .

[71] May-Newman, K. and F. Yin. 1998. A constitutive law for mitral valve tissue. *Journal of Biomechanical Engineering* 120: 38–47 .

[72] Meek, K.M., T. Blamires, G.F. Elliott, T.J. Gyi, and C. Nave. 1987. The organisation of collagen fibrils in the human corneal stroma: A synchrotron x-ray diffraction study. *Current Eye Research 6*(7): 841–846 .

[73] Mehnert, M., M. Hossain, and P. Steinmann. 2021a. A comprehensive thermo-electro-viscoelastic characterization of electro-active polymers - part i: Experimental investigations. *Journal of the Mechanics and Physics of Solids* 157: 104603 .

[74] Mehnert, M., M. Hossain, and P. Steinmann. 2021b. A comprehensive thermo-electro-viscoelastic characterization of electro-active polymers - part ii: Continuum modeling approach. *Journal of the Mechanics and Physics of Solids* 157: 104625 .

[75] Melnik, A.V., H. Borja Da Rocha, and A. Goriely. 2015. On the modeling of fiber dispersion in fiber-reinforced elastic materials. *International Journal of Non-Linear Mechanics* 75: 92–106 .

[76] Mihai, L.A., L. Chin, P.A. Janmey, and A. Goriely. 2015. A comparison of hyperelastic constitutive models applicable to brain and fat tissues. *Journal of The Royal Society Interface 12*(110): 20150486 .

[77] Murphy, J. 2013. Transversely isotropic biological, soft tissue must be modelled using both anisotropic invariants. *European Journal of Mechanics-A/Solids* 42: 90–96 .

[78] Myers, K., S. Socrate, A. Paskaleva, and M. House. 2010. A study of the anisotropy and tension/compression behavior of human cervical tissue. *Journal of Biomechanical Engineering 132*(2): 021003 .

[79] Niestrawska, J.A., C. Viertler, P. Regitnig, T.U. Cohnert, G. Sommer, and G.A. Holzapfel. 2016. Microstructure and mechanics of healthy and aneurysmatic abdominal aortas: experimental analysis and modelling. *Journal of The Royal Society Interface 13*(124): 20160620 .

[80] Ogden, R.W. and G. Saccomandi. 2007. Introducing mesoscopic information into constitutive equations for arterial walls. *Biomechanics and Modeling in Mechanobiology 6*(5): 333–344 .

[81] Pai, S. and W.R. Ledoux. 2010. The compressive mechanical properties of diabetic and non-diabetic plantar soft tissue. *Journal of Biomechanics 43*(9): 1754–1760 .

[82] Pandolfi, A. and M. Vasta. 2012. Fiber distributed hyperelastic modeling of biological tissues. *Mechanics of Materials* 44: 151–162 .

[83] Sacks, M.S. 2003. Incorporation of experimentally-derived fiber orientation into a structural constitutive model for planar collagenous tissues. *J. Biomech. Eng. 125*(2): 280–287 .

[84] Schriefl, A.J., H. Wolinski, P. Regitnig, S.D. Kohlwein, and G.A. Holzapfel. 2013. An automated approach for three-dimensional quantification of fibrillar structures in optically cleared soft biological tissues. *Journal of The Royal Society Interface 10*(80): 20120760 .

[85] Schriefl, A.J., G. Zeindlinger, D.M. Pierce, P. Regitnig, and G.A. Holzapfel. 2012. Determination of the layer-specific distributed collagen fibre orientations in human thoracic and abdominal aortas and common iliac arteries. *Journal of the Royal Society Interface 9*(71): 1275–1286 .

[86] Sommer, G., S. Sherifova, P.J. Oberwalder, O.E. Dapunt, P.A. Ursomanno, A. DeAnda, B.E. Griffith, and G.A. Holzapfel. 2016. Mechanical strength of aneurysmatic and dissected human thoracic aortas at different shear loading modes. *Journal of Biomechanics 49*(12): 2374–2382 .

[87] Steinmann, P., M. Hossain, and G. Possart. 2012. Hyperelastic models for rubber-like materials: consistent tangent operators and suitability for treloar's data. *Archive of Applied Mechanics 82*(9): 1183–1217 .

[88] Takamizawa, K. and K. Hayashi. 1987. Strain energy density function and uniform strain hypothesis for arterial mechanics. *Journal of biomechanics 20*(1): 7–17 .

[89] Tong, P. and Y.C. Fung. 1976. The stress-strain relationship for the skin. *Journal of Biomechanics 9*(10): 649–657 .

[90] Treloar, L. 1943. The elasticity of a network of long-chain molecules. i. *Transactions of the Faraday Society* 39: 36–41 .

[91] Untaroiu, C.D., Y.C. Lu, S.K. Siripurapu, and A.R. Kemper. 2015. Modeling the biomechanical and injury response of human liver parenchyma under tensile loading. *Journal of the Mechanical Behavior of Biomedical Materials* 41: 280–291 .

[92] Vaishnav, R.N., J.T. Young, and D.J. Patel. 1973. Distribution of stresses and of strain-energy density through the wall thickness in a canine aortic segment. *Circulation research 32*(5): 577–583 .

[93] Vignali, E., E. Gasparotti, K. Capellini, B.M. Fanni, L. Landini, V. Positano, and S. Celi. 2021. Modeling biomechanical interaction between soft tissue and soft robotic instruments: importance of constitutive anisotropic hyperelastic formulations. *The International Journal of Robotics Research 40*(1): 224–235 .

[94] Weiss, J.A., B.N. Maker, and S. Govindjee. 1996. Finite element implementation of incompressible, transversely isotropic hyperelasticity. *Computer methods in applied mechanics and engineering 135*(1-2): 107–128 .

[95] Wex, C., S. Arndt, A. Stoll, C. Bruns, and Y. Kupriyanova. 2015. Isotropic incompressible hyperelastic models for modelling the mechanical behaviour of biological tissues: a review. *Biomedical Engineering 60*(6): 577–592 .

[96] Zulliger, M.A., P. Fridez, K. Hayashi, and N. Stergiopulos. 2004. A strain energy function for arteries accounting for wall composition and structure. *Journal of biomechanics 37*(7): 989–1000 .

Appendix

Root mean square error (RMSE) can be used as an alternative quality of fit metric to compare the performance of models. RSME for uniaxial dataset of Cooney et al. [19], and Martins et al. [70] is

$$\mathrm{RMSE} = \sqrt{\frac{\sum\limits_{i=1}^{n_{UT_1}} \left(P_{11}^{UT_1}(\lambda_i) - P_{11}^{exp,UT_1}(\lambda_i)\right)^2}{n_{UT_1}}} + \sqrt{\frac{\sum\limits_{i=1}^{n_{UT_2}} \left(P_{22}^{UT_2}(\lambda_i) - P_{22}^{exp,UT_2}(\lambda_i)\right)^2}{n_{UT_2}}}. \tag{101}$$

Similarly, for the equibiaxial loading case, RMSE for the dataset of Niestrawska et al. [79] is

$$\mathrm{RMSE} = \sqrt{\frac{\sum\limits_{i=1}^{n_{ET}} \left(P_{11}^{ET}(\lambda_i) - P_{11}^{exp,ET}(\lambda_i)\right)^2}{n_{ET}}} + \sqrt{\frac{\sum\limits_{i=1}^{n_{ET}} \left(P_{22}^{ET}(\lambda_i) - P_{22}^{exp,ET}(\lambda_i)\right)^2}{n_{ET}}}. \tag{102}$$

Another quality of fit metric is the coefficient of determination (R^2). R^2 for uniaxial dataset of Cooney et al. [19], and Martins et al. [70] is

$$R^2 = 0.5\left[1 - \frac{\sum\limits_{i=1}^{n_{UT_1}} \left(P_{11}^{UT_1}(\lambda_i) - P_{11}^{exp,UT_1}(\lambda_i)\right)^2}{\sum\limits_{i=1}^{n_{UT_1}} \left(P_{11}^{UT_1}(\lambda_i) - \mathrm{mean}(P_{11}^{exp,UT_1}(\lambda_i))\right)^2}\right] + 0.5\left[1 - \frac{\sum\limits_{i=1}^{n_{UT_2}} \left(P_{22}^{UT_2}(\lambda_i) - P_{22}^{exp,UT_2}(\lambda_i)\right)^2}{\sum\limits_{i=1}^{n_{UT_2}} \left(P_{22}^{UT_2}(\lambda_i) - \mathrm{mean}(P_{22}^{exp,UT_2}(\lambda_i))\right)^2}\right]. \tag{103}$$

Similarly, for equibiaxial loading case, R^2 for the fitting of dataset of Niestrawska et al. [79] is

$$R^2 = 0.5\left[1 - \frac{\sum\limits_{i=1}^{n_{ET}} \left(P_{11}^{ET}(\lambda_i) - P_{11}^{exp,ET}(\lambda_i)\right)^2}{\sum\limits_{i=1}^{n_{ET}} \left(P_{11}^{ET}(\lambda_i) - \mathrm{mean}(P_{11}^{exp,ET}(\lambda_i))\right)^2}\right] + 0.5\left[1 - \frac{\sum\limits_{i=1}^{n_{ET}} \left(P_{22}^{ET}(\lambda_i) - P_{22}^{exp,ET}(\lambda_i)\right)^2}{\sum\limits_{i=1}^{n_{ET}} \left(P_{22}^{ET}(\lambda_i) - \mathrm{mean}(P_{22}^{exp,ET}(\lambda_i))\right)^2}\right]. \tag{104}$$

Table 3 Models sorted according to the *root mean square error* to the equibiaxial dataset of AAA tissue [79], uniaxial dataset of the linea alba [19] and uniaxial dataset of the rectus sheath [70].

	AAA tissue				**linea alba**				**rectus sheath**			
rank	**model name**	**model type**	RMSE	*nop*	**model name**	**model type**	RMSE	*nop*	**model name**	**model type**	RMSE	*nop*
1	HNORS model [46]	GST	0.8640	6	ARCCH model [4]	AI	0.1523	6	ARCCH model [4]	AI	0.0321	6
2	HSGR model [50]	I_1, I_4	0.8566	5	HY model [56]	I_1, I_4	0.1605	4	NY model [71]	I_1, I_4	0.0405	4
3	AMDM model [1]	AI	0.8632	5	AMDM model [1]	AI	0.1646	5	OS model [80]	I_1, I_4	0.0459	6
4	LOH model [69]	AI	0.8801	5	ASMD model [2]	AI	0.1646	6	HY model [56]	I_1, I_4	0.0986	4
5	GOH model [34]	GST	0.9208	5	OS model [80]	I_1, I_4	0.1857	6	LOH model [69]	AI	0.1047	5
6	HY model [56]	I_1, I_4	1.0216	4	DBB model [24]	AI	0.1951	6	ASMD model [2]	AI	0.1051	6
7	NY model [71]	I_1, I_4	1.0613	4	HSGR model [50]	I_1, I_4	0.1981	5	AMDM model [1]	AI	0.1099	5
8	ASMD model [2]	AI	1.5261	6	LOH model [69]	AI	0.2055	5	DBB model [24]	AI	0.1673	6
9	HGO model [44]	I_1, I_4	1.5503	4	GOH model [34]	GST	0.2167	4	HSGR model [50]	I_1, I_4	0.3633	5
10	ARCCH model [4]	AI	2.1963	6	HGO model [44]	I_1, I_4	0.2196	4	HGO model [44]	I_1, I_4	0.3805	4
11	DBB model [24]	AI	3.1565	6	HNORS model [46]	GST	0.2350	6	GOH model [34]	GST	0.3887	4
12	OS model [80]	I_1, I_4	3.5456	5	NY model [71]	I_1, I_4	1.0339	4	HNORS model [46]	GST	0.3893	6

Table 4 Models sorted according to the *coefficient of determination* to the equibiaxial dataset of AAA tissue [79], uniaxial dataset of the linea alba [19] and uniaxial dataset of the rectus sheath [70].

	AAA tissue				**linea alba**				**rectus sheath**			
rank	**model name**	**model type**	R^2	*nop*	**model name**	**model type**	R^2	*nop*	**model name**	**model type**	R^2	*nop*
1	HNORS model [46]	GST	0.9976	6	ARCCH model [4]	AI	0.9952	6	ARCCH model [4]	AI	0.9987	6
2	HSGR model [50]	I_1, I_4	0.9976	5	HY model [56]	I_1, I_4	0.9949	4	NY model [71]	I_1, I_4	0.9940	4
3	AMDM model [1]	AI	0.9976	5	AMDM model [1]	AI	0.9935	5	HY model [56]	I_1, I_4	0.9873	4
4	LOH model [69]	AI	0.9975	5	ASMD model [2]	AI	0.9935	6	LOH model [69]	AI	0.9862	5
5	GOH model [34]	GST	0.9972	5	OS model [80]	I_1, I_4	0.9932	6	ASMD model [2]	AI	0.9859	6
6	NY model [71]	I_1, I_4	0.9955	4	LOH model [69]	AI	0.9914	5	AMDM model [1]	AI	0.9848	5
7	HY model [56]	I_1, I_4	0.9952	4	DBB model [24]	AI	0.9876	6	OS model [80]	I_1, I_4	0.9822	6
8	ASMD model [2]	AI	0.9935	6	HSGR model [50]	I_1, I_4	0.9738	5	DBB model [24]	AI	0.9405	6
9	ARCCH model [4]	AI	0.9842	6	GOH model [34]	GST	0.9730	4	HSGR model [50]	I_1, I_4	0.2631	5
10	HGO model [44]	I_1, I_4	0.9708	4	HGO model [44]	I_1, I_4	0.9729	4	HGO model [44]	I_1, I_4	0.2114	4
11	DBB model [24]	AI	0.9698	6	HNORS model [46]	GST	0.9721	6	GOH model [34]	GST	0.1396	4
12	OS model [80]	I_1, I_4	0.9635	5	NY model [71]	I_1, I_4	0.7574	4	HNORS model [46]	GST	0.1396	6

Table 5 Identified parameters and error bounds based on AAA tissue dataset

	NY model					HGO model					HSGR model				
Parameters	$k_0 = 0.1148\ [MPa]$ $k_1 = 31.1439$ $k_2 = 1.5230e+03$ $\varphi = 26°$					$\mu = 2.6712\ [MPa]$ $k_1 = 0.1742\ [MPa]$ $k_2 = 55.9001$ $\varphi = 26°$					$\mu = 0.9347\ [MPa]$ $k_1 = 0.2704\ [MPa]$ $k_2 = 47.0232$ $\varphi = 26°$ $p = 0.9126$				
			Quality of fit					Quality of fit					Quality of fit		
	Weight	Error	Region 1	Region 2	Region 3	Weight	Error	Region 1	Region 2	Region 3	Weight	Error	Region 1	Region 2	Region 3
ET-axial	0.1665	0.2941	0.0000	7.7801	8.1602	0.1	2.4033	0.0000	7.5929	13.3316	0.1	0.1255	0	1.0337	1.4823
ET-circ.	0.8335	0.2693	1.5845	0	2.9212	0.9000	14.1329	8.7405	0	34.1676	0.9	0.2524	0.2511	1.0337	0.9911
Total	1.0000	0.5634	1.5845	7.7801	11.0814	1.0000	16.5362	8.7405	7.5929	47.4992	1.0000	0.3779	0.2511	1.0337	2.4734
	OS model					DBB model					GOH model				
Parameters	$\mu = 2.5537\ [MPa]$ $k_1 = 3.38107\ [MPa]$ $J_h = 0.1149$ $J_m = 0.2369$ $\varphi = 26°$					$G = 2.1366\ [MPa]$ $k_1 = 3.1017\ [MPa]$ $k_2 = 46.8793$ $\varphi = 26°$ $\sigma = 0.2597$ $\phi_{tot} = 0.7000$					$\mu = 1.7416\ [MPa]$ $k_1 = 4.4460\ [MPa]$ $k_2 = 161.3920\ [MPa]$ $\varphi = 26°$ $\kappa = 0.2256$				
			Quality of fit					Quality of fit					Quality of fit		
	Weight	Error	Region 1	Region 2	region 3	Weight	Error	Region 1	Region 2	region 3	Weight	Error	Region 1	Region 2	Region 3
ET-axial	0.1	1.3169	0	3.7799	10.4829	0.1000	1.2764	0.5860	0.7356	3.5558	0.1000	0.1377	0	1.2187	1.6822
ET-circ.	0.9000	5.7514	16.3691	0	75.6493	0.9000	4.1076	0.4600	2.0767	7.2367	0.9000	0.3022	0.2795	0	1.6821
Total	1.0000	7.0679	16.3691	3.7799	86.1323	1.0000	5.3840	1.0460	2.8123	10.7926	1.0000	0.4399	0.2795	1.2187	3.3643
	AMDM model					ASMD model					HNORS model				
Parameters	$mu = 0.9337\ [MPa]$ $k_1 = 0.9118\ [MPa]$ $k_2 = 46.8474$ $\varphi = 26°$ $b = 3.67$					$\mu = 0.6517\ [MPa]$ $k_1 = 3.5475\ [MPa]$ $k_2 = 46.4817$ $\kappa_1 = 2.3798e-07$ $\kappa_2 = 0.9$ $\kappa_3 = 0$					$\mu = 1.8517\ [MPa]$ $k_1 = 0.6981\ [MPa]$ $k_2 = 59.9093$ $\kappa_{ip} = 0.7657$ $\kappa_{op} = 0.47$ $\varphi = 26°$				
			Quality of fit					Quality of fit					Quality of fit		
	Weight	Error	Region 1	Region 2	Region 3	Weight	Error	Region 1	Region 2	Region 3	Weight	Error	Region 1	Region 2	Region 3
ET-axial	0.9000	0.1241	0	1.0682	1.4882	0.9000	0.1757	0	1.9907	2.5057	0.1000	0.1249	0	1.0843	1.5269
ET-circ.	0.1000	0.2610	0.3232	0	1.3659	0.1000	1.2253	0.0642	0	1.2907	0.9000	0.2429	0.2309	0	0.9099
Total	1.0000	0.3851	0.3232	1.0682	2.8541	1.0000	1.4010	0.0642	1.9907	3.7984	1.0000	0.3675	0.2309	1.0843	2.4368
	LOH model					ARCCH model					HY model				
Parameters	$\mu = 0.9753\ [MPa]$ $k_1 = 1.1214$ $k_2 = 50.6635$ $\varphi = 26°$ $b = 1.1204$					$\xi_1 = 0.9753\ [MPa]$ $\xi_2 = 7787.6$ $\xi_3 = 634$ $\alpha_1 = 8.387$ $\alpha_2 = 8.1206$ $\alpha_3 = 3.4849$ $\varphi = 26°$					$c = 0.0090079\ [MPa]$ $b = 20.436$ $A = 0.0013501$ $a = 239.78$ $\varphi = 26°$				
			Quality of fit					Quality of fit					Quality of fit		
	Weight	Error	Region 1	Region 2	Region 3	Weight	Error	Region 1	Region 2	Region 3	Weight	Error	Region 1	Region 2	Region 3
ET-axial	0.9900	0.1258	0.5868	0.8817	1.3442	0.97916	1.683	2.3532	7.5913	10.599	0.9900	0.19141	0.97455	2.2538	2.4671
ET-circ.	0.0100	0.2761	0.3193	0.7885	1.1503	0.020836	0.80819	4.1569	12.635	14.579	0.0100	0.34122	2.9966	6.9173	7.6985
Total	1.0000	0.4019	0.9061	1.6702	2.4945	1.0000	2.4912	6.51	20.226	20.179	1.0000	0.53263	3.9712	9.1710	10.1660

Table 6 Identified parameters and error bounds based on LA tissue dataset

	NY model					HGO model					HSGR model				
Parameters	$k_0 = 2.9076e+03$ $[MPa]$ $k_1 = 0.0028$ $k_2 = 0.8380$ $\varphi = 0°$					$\mu = 1.1586$ $[MPa]$ $k_1 = 8.6064$ $[MPa]$ $k_2 = 11.4196$ $\varphi = 0°$					$\mu = 1.1525$ $[MPa]$ $k_1 = 87.4399$ $[MPa]$ $k_2 = 5.0524$ $\varphi = 0°$ $p = 0.0458$				
			Quality of fit					Quality of fit					Quality of fit		
	Weight	Error	Region 1	Region 2	Region 3	Weight	Error	Region 1	Region 2	Region 3	Weight	Error	Region 1	Region 2	Region 3
UT-trans.	0.1000	0.0399	0.6616	1.5653	1.7889	0.1000	0.0079	0.3335	0.4445	0.4892	0.1001	0.0079	0.3337	0.4448	0.4895
UT-circ.	0.9000	0.6957	2.6033	8.3558	9.5460	0.9000	0.0171	0.7246	0.7392	0.7637	0.8999	0.0123	0.5304	0.5411	0.5573
Total	1.0000	0.7356	3.2648	9.9211	11.3349	1.0000	0.0250	1.0581	1.1837	1.2529	1.0000	0.0199	0.8641	0.9859	1.0468
	OS model					DBB model					GOH model				
Parameters	$\mu = 1.7592$ $[MPa]$ $k_1 = 9.8814$ $[MPa]$ $J_h = 0.2883$ $J_m = 0.0944$ $\varphi = 0°$					$G = 0.0500$ $[MPa]$ $k_1 = 56.0009$ $[MPa]$ $k_2 = 0.7921$ $\varphi = 0°$ $\sigma = 0.4985$ $\phi_{tot} = 0.5200$					$\mu = 2.3048$ $[MPa]$ $k_1 = 17.2552$ $[MPa]$ $k_2 = 20.5490$ $[MPa]$ $\varphi = 0°$ $\kappa = 0.0998$				
			Quality of fit					Quality of fit					Quality of fit		
	Weight	Error	Region 1	Region 2	region 3	Weight	Error	Region 1	Region 2	region 3	Weight	Error	Region 1	Region 2	Region 3
UT-trans.	0.1000	$8.4265e-04$	0.0709	0.0736	0.0797	0.0100	0.0030	0.0140	0.0754	0.1022	0.1000	0.0076	0.0335	0.4444	0.4892
ET-circ.	0.9000	0.0245	0.9835	1.0114	1.0496	0.9900	0.0199	0.8302	0.8902	0.8980	0.9000	0.0164	0.6971	0.7106	0.7336
Total	1.0000	0.0253	1.0544	1.0851	1.1294	1.0000	0.0299	0.8441	0.9656	1.0002	1.0000	0.024	1.0306	1.1551	1.2228
	AMDM model					ASMD model					HNORS model				
Parameters	$mu = 0.7418$ $[MPa]$ $k_1 = 15.3359$ $[MPa]$ $k_2 = 10.6226$ $\varphi = 0°$ $b = 2.6374$					$\mu = 0.7420$ $[MPa]$ $k_1 = 15.6560$ $[MPa]$ $k_2 = 10.6286$ $\kappa_1 = 4.999e-07$ $\kappa_2 = 5.2757$ $\kappa_3 = 0.0000$					$\mu = 2.3050$ $[MPa]$ $k_1 = 270.6246$ $[MPa]$ $k_2 = 5.0500$ $\kappa_{ip} = 0.6448$ $\kappa_{op} = 0.4999$ $\varphi = 0°$				
			Quality of fit					Quality of fit					Quality of fit		
	Weight	Error	Region 1	Region 2	Region 3	Weight	Error	Region 1	Region 2	Region 3	Weight	Error	Region 1	Region 2	Region 3
UT-trans.	0.1000	0.0012	0.0800	0.0843	0.0944	0.1000	0.0012	0.0800	0.0844	0.0944	0.8998	0.0076	0.3255	0.4304	0.4789
UT-circ.	0.9000	0.0170	0.7877	0.8052	0.8219	0.9000	0.0170	0.7873	0.0847	0.8214	0.1002	0.0055	0.2138	0.2221	0.2286
Total	1.0000	0.0182	0.8677	0.8895	0.9163	1.0000	0.0182	0.8673	0.8890	0.9159	1.0000	0.0131	0.5494	0.6525	0.7075
	LOH model					ARCCH model					HY model				
Parameters	$\mu = 0.7419$ $[MPa]$ $k_1 = 16.8000$ $k_2 = 10.6200$ $\varphi = 0°$ $b = 2.6800$					$\xi_1 = 499.78$ $[MPa]$ $\xi_2 = 0.26603$ $\xi_3 = 5.6874$ $\alpha_1 = 2.1792$ $\alpha_2 = 2.0002$ $\alpha_3 = 2.0031$ $\varphi = 0°$					$c = 0.19046$ $[MPa]$ $b = 4.5563$ $A = 0.31734$ $a = 58.719$ $\varphi = 0°$				
			Quality of fit					Quality of fit					Quality of fit		
	Weight	Error	Region 1	Region 2	Region 3	Weight	Error	Region 1	Region 2	Region 3	Weight	Error	Region 1	Region 2	Region 3
UT-trans.	0.9900	0.0012	0.0693	0.0725	0.0849	0.010496	0.00061	0.001011	0.010532	0.017146	0.010036	0.000625	0.054814	0.056258	0.060844
UT-circ.	0.0100	0.0294	0.7412	0.7634	0.8578	0.9895	0.016284	0.31968	0.35238	0.39644	0.98996	0.018358	0.76986	0.78612	0.81305
Total	1.0000	0.0306	0.8104	0.8358	0.9427	1.0000	0.016896	0.32069	0.36291	0.41359	1.0000	0.018983	0.82467	0.84238	0.8739

Table 7 Identified parameters and error bounds based on RS tissue dataset

	NY model					HGO model					HSGR model				
Parameters	$k_0 = 0.8366\ [MPa]$ $k_1 = 6.3492$ $k_2 = 25.7852$ $\varphi = 90°$					$\mu = 0.0700\ [MPa]$ $k_1 = 0.4465\ [MPa]$ $k_2 = 7.6186$ $\varphi = 90°$					$\mu = 0.0900\ [MPa]$ $k_1 = 3.1260\ [MPa]$ $k_2 = 35.2661$ $\varphi = 90°$ $p = 0.1000$				
			Quality of fit					Quality of fit					Quality of fit		
	Weight	Error	Region 1	Region 2	Region 3	Weight	Error	Region 1	Region 2	Region 3	Weight	Error	Region 1	Region 2	Region 3
UT-longi.	0.1015	$2.7021e-04$	0.0252	0.0279	0.0287	0.1000	0.0059	0.9175	1.0585	1.0908	0.1000	0.0048	0.7407	0.8783	0.9004
UT-trans.	0.8985	$6.8242e-04$	0.0275	0.0557	0.0663	0.9000	0.0981	0.0122	0.4693	2.6674	0.9000	0.0863	0.0059	0.3937	2.4541
Total	1.0000	$9.5263e-04$	0.0526	0.0836	0.0949	1.0000	0.0981	0.9297	1.5278	3.7582	1.0000	0.0911	0.7467	1.2720	3.3545
	OS model					DBB model					GOH model				
Parameters	$\mu = 0.6971\ [MPa]$ $k_1 = 0.3315\ [MPa]$ $J_h = 0.1381$ $J_m = 0.3263$ $\varphi = 90°$					$G = 0.05\ [MPa]$ $k_1 = 9.0099\ [MPa]$ $k_2 = 5.0009$ $\varphi = 90°$ $\sigma = 1.0473$ $\phi_{tot} = 0.3001$					$\mu = 0.0700\ [MPa]$ $k_1 = 23.5547\ [MPa]$ $k_2 = 131.2277\ [MPa]$ $\varphi = 90°$ $\kappa = 0.2500$				
			Quality of fit					Quality of fit					Quality of fit		
	Weight	Error	Region 1	Region 2	region 3	Weight	Error	Region 1	Region 2	region 3	Weight	Error	Region 1	Region 2	Region 3
ET-axial	0.9000	0.0173	2.2566	2.6379	2.7472	0.9900	0.0082	1.2097	1.54155	1.5579	0.0100	0.0037	0.4653	0.5722	0.5904
ET-circ.	0.1000	0.0021	0.4551	0.6240	0.6351	0.0100	0.0059	0.1067	0.1365	0.2762	0.9900	0.1033	0.0365	0.6314	3.0817
Total	1.0000	0.0194	2.7117	3.2618	3.3823	1.0000	0.0141	1.3164	1.6780	1.8341	1.0000	0.1059	0.5019	1.2036	3.6722
	AMDM model					ASMD model					HNORS model				
Parameters	$mu = 1.8478e-05\ [MPa]$ $k_1 = 3.1303\ [MPa]$ $k_2 = 9.3118$ $\varphi = 90°$ $b = 0.2620$					$\mu = 0.0503\ [MPa]$ $k_1 = 1.9067\ [MPa]$ $k_2 = 13.5294$ $\kappa_1 = 6.3935e-07$ $\kappa_2 = 8.9346e-07$ $\kappa_3 = 0$					$\mu = 0.0851\ [MPa]$ $k_1 = 16.7116\ [MPa]$ $k_2 = 152.3987$ $\kappa_{ip} = 0.5217$ $\kappa_{op} = 0.3900$ $\varphi = 90°$				
			Quality of fit					Quality of fit					Quality of fit		
	Weight	Error	Region 1	Region 2	Region 3	Weight	Error	Region 1	Region 2	Region 3	Weight	Error	Region 1	Region 2	Region 3
Axial	0.9000	0.0065	.4221	0.4869	0.5097	0.9000	0.0347	0.0757	0.1804	0.4085	0.8999	0.0051	0.4923	0.5730	0.6161
ET-circ.	0.1000	$9.1167e-04$	0.1763	0.2386	0.2466	0.1000	0.0024	0.1200	0.1478	0.1925	0.1001	0.1008	0.0299	0.5931	2.9878
Total	1.0000	$7.41167e-03$	0.5984	0.7254	0.7563	1.0000	0.0371	0.1957	0.3282	0.6011	1.0000	0.1059	0.5221	1.1661	3.6038
	LOH model					ARCCH model					HY model				
Parameters	$\mu = 0.0001\ [MPa]$ $k_1 = 3.0203$ $k_2 = 10.4480$ $\varphi = 90°$ $b = 0.2756$					$\xi_1 = 3.5493\ [MPa]$ $\xi_2 = 0.45369$ $\xi_3 = 0.32705$ $\alpha_1 = 3.5004$ $\alpha_2 = 2.8566$ $\alpha_3 = 3.9793$ $\varphi = 90°$					$c = 0.01466\ [MPa]$ $b = 16.238$ $A = 0.0087704$ $a = 41.554$ $\varphi = 90°$				
			Quality of fit					Quality of fit					Quality of fit		
	Weight	Error	Region 1	Region 2	Region 3	Weight	Error	Region 1	Region 2	Region 3	Weight	Error	Region 1	Region 2	Region 3
UT-trans.	0.0101	0.0057	0.7220	0.8291	0.8697	0.98372	0.0005274	0.04557	0.052665	0.056817	0.98984	0.0048681	0.77239	0.88319	0.9104
UT-circ.	0.9899	$8.4280e-04$	0.1486	0.1953	0.2054	0.016284	$8.4362e-05$	0.0018366	0.0059022	0.0073888	0.010159	0.00083176	0.15862	0.19895	0.20977
Total	1.0000	0.0066	0.8705	1.0244	1.0750	1.0000	0.00061176	0.047406	0.058568	0.064206	1.0000	0.0056999	0.93101	1.0821	1.1202